NONLINEAR STRONG SHOCK INTERACTIONS:
A SHOCK-FITTED APPROACH

G. Erlebacher, M.Y. Hussaini

Program in Computational Science and Engineering

Florida State University, Tallahassee, FL 32306-3075.

and T.L. Jackson

Institute for Computer Applications in Science and Engineering

NASA Langley Research Center, Hampton, VA 23681-0001.

ABSTRACT

This paper addresses nonlinear effects which result from the interaction of shock waves with vortices. A series of experiments are carried out, which involve the interaction of a strong shock wave with a single plane vorticity wave and a randomly distributed wave system. These experiments are first conducted in the linear regime to obtain a mutual verification of theory and computation. They are subsequently extended into the nonlinear regime. A systematic study of the interaction of a plane shock wave and a single vortex is then conducted. Specifically, we investigate the conditions under which nonlinear effects become important, both as a function of shock Mach number, M_1, and incident vortex strength (characterized by its circulation Γ). The shock Mach number is varied from 2 to 8, while the circulation of the vortex is varied from infinitesimally small values (linear theory) to unity. Budgets of vorticity, dilatation, and pressure are obtained. They indicate that nonlinear effects become more significant as both the shock Mach number and the circulation increase. For Mach numbers equal to 5 and above, the dilatation in the vortex core grows quadratically with circulation. An acoustic wave propagates radially outwards from the vortex center. As circulation increases, its upstream-facing front steepens at low Mach numbers, and its

downstream-facing front steepens at high Mach numbers. A high-Mach number asymptotic expansion of the Rankine-Hugoniot conditions reveals that nonlinear effects dominate both the shock motion and the downstream flow for $\Gamma M_1 > 1$.

1 Introduction

Our understanding of the turbulence alteration mechanisms underlying shock interaction phenomena is far from complete, particularly those phenomena dominated by nonlinearities. To help elucidate some of the nonlinear mechanisms, this work concentrates on the cases of high shock Mach number and large amplitude disturbances.

As a turbulent velocity field could be represented as a linear combination of plane sinusoidal vorticity or shear waves of all orientations and wavelengths, Ribner (1953) was motivated to analyze a single arbitrary plane shear wave convected through a plane shock. Then, he Fourier synthesized the modified individual waves downstream of the shock to obtain, in particular, results on noise generation due to interaction of a shock with turbulence (Ribner 1954, 1987). Other early studies of a single wave passing through a shock are those of Moore (1953), Chang (1957) and Kerrebrock (1956). They linearized the Euler equations and the Rankine-Hugoniot conditions, and were able to parametrize the properties of the downstream vortical, acoustic, and entropy waves as a function of the upstream wave angle and the shock Mach number.

The initial numerical computations of a single wave interacting with a shock are due to Zang, Hussaini & Bushnell (1984). They compared their numerical results with the predictions of the linear theory (McKenzie & Westphal 1968), and placed some limits on its range of validity. They confirmed the validity of linear theory in two of its three questionable regimes — weak shocks and strong disturbances; there was serious discrepancy between numerical results and the linear predictions for the third regime — waves with incidence in the neighborhood of the critical angle which demarcates, according to linear theory, the region of constant amplitude plane pressure waves behind the shock from the region of exponentially decaying ones. Zang *et al.* (1984) found discrepancies between the numerical results and linear theory as the critical angle was approached. The largest errors were on the supercritical side. Lasseigne, Jackson & Hussaini (1991) suggested that the apparent discrepancy between linear theory and numerical computations would disappear for angles close to critical if the simulation time were long enough for the transients to decay. However, the expense of their numerical algorithm prevented extensive checking of this hypothesis. We address this issue herein, and confirm the hypothesis.

Turbulent flow fields are usually surmised to consist of large-scale coherent structures and fine-grained turbulence. Vortex dynamics approach to turbulence studies such coherent or organized structures by assuming an assembly of vortical states represented by vortices, vortex rings, or vortex sheets (Saffman 1985). To study in isolation the mechanism of noise generation due to coherent structures interacting with a shock, Ram & Ribner (1957) and Ribner (1985) investigated the properties of a lateral vortex passing through a shock by Fourier-decomposing the vortex, letting each component (or wave) interact with the shock, and recombining the resulting waves downstream. They obtained analytical expressions for the expanding cylindrical acoustic front (which forms as the shock intersects the vortex) centered at the transmitted vortex. These results were later confirmed by experimental observations (Weeks & Dosanjh 1965, 1967, Naumann & Hermanns 1973). The first numerical study of shock/vortex interaction is that of Pao & Salas (1981). Their approach is based on finite-difference discretization of the Euler equations with a fitted shock at the inflow boundary. Salas, Zang & Hussaini (1982) applied shock-fitted pseudospectral techniques to treat problems in which a single vortex, a vortex street, and an entropy spot interact with a shock. Results demonstrated qualitative agreement with the experimental observations of Weeks & Dosanjh (1965). Further numerical work includes recent studies of Meadows, Kumar & Hussaini (1991), Meadows (1995), and Ellzey *et al.* (1995).

The present study focuses on the nonlinear aspects of a shock interacting with plane vorticity waves of infinitesimal amplitude, with a random collection of these vorticity waves, and with a Burgers vortex. We solve the Euler equations using high-order finite-difference algorithms which fit the shock. A simple, yet efficient, absorbing outflow boundary condition permits accurate long-time integrations. The accuracy and efficiency of the computational model allows one to distinguish the discrepancies due to transient phenomena from the errors due to insufficient resolution of the upstream waves. After establishing the conditions under which upstream waves generate accurate stationary statistical time averages, we construct an ensemble of waves in the upstream domain, which are then convected through the shock. After imposing a particular energy spectrum on the upstream flow, we compare the downstream spectra of velocity, dilatation, and vorticity with theoretical linear predictions, both in the linear and the nonlinear regimes. Finally, we consider the interaction of a single vortex with a shock at Mach numbers ranging from 2 through 8, and over a wide range of vortex amplitudes. Using asymptotic theory, we then establish quantitatively the conditions under which linear theory is expected to break down.

The paper is organized as follows. Section 2 contains the mathematical formulation of the problem. Section 3 provides the details of the numerical method. Results from the computations and comparisons with linear theory are presented in section 4. The problem of a shock interacting with a vortex is presented in section 5. Finally, conclusions are drawn in section 7.

2 Problem Formulation

We consider the motion of a perfect gas in an infinite medium with an initial infinite plane shock. We assume that the two-dimensional compressible Euler equations (in a Cartesian coordinate system)

$$\frac{\partial \rho}{\partial t} + \rho \left[\frac{\partial u}{\partial x} + \frac{\partial v}{\partial y} \right] + u\frac{\partial \rho}{\partial x} + v\frac{\partial \rho}{\partial y} = 0, \tag{1}$$

$$\frac{\partial u}{\partial t} + u\frac{\partial u}{\partial x} + v\frac{\partial u}{\partial y} = -\frac{1}{\rho}\frac{\partial p}{\partial x}, \tag{2}$$

$$\frac{\partial v}{\partial t} + u\frac{\partial v}{\partial x} + v\frac{\partial v}{\partial y} = -\frac{1}{\rho}\frac{\partial p}{\partial y}, \tag{3}$$

$$\frac{\partial p}{\partial t} + u\frac{\partial p}{\partial x} + v\frac{\partial p}{\partial y} = -\gamma p \left[\frac{\partial u}{\partial x} + \frac{\partial v}{\partial y} \right], \tag{4}$$

govern the flow upstream and downstream of the shock. The equation of state for an ideal gas, $p = \rho T$, is implicit in the derivation. These equations are nondimensional; the variables are scaled with respect to the initial upstream state. Thus, the pressure, and density are referred to p_0 and ρ_0, respectively, where the subscript 0 denotes dimensional values upstream of the shock. Velocities are referred to $(p_0/\rho_0)^{1/2}$, lengths are referred to an arbitrary length scale L_0, and time is referred to the ratio of length and velocity scales. The ratio of specific heats, γ, is assumed to be 1.4. The upstream variables carry a subscript 1 to distinguish them from the downstream ones. The geometry is illustrated in Figure 1.

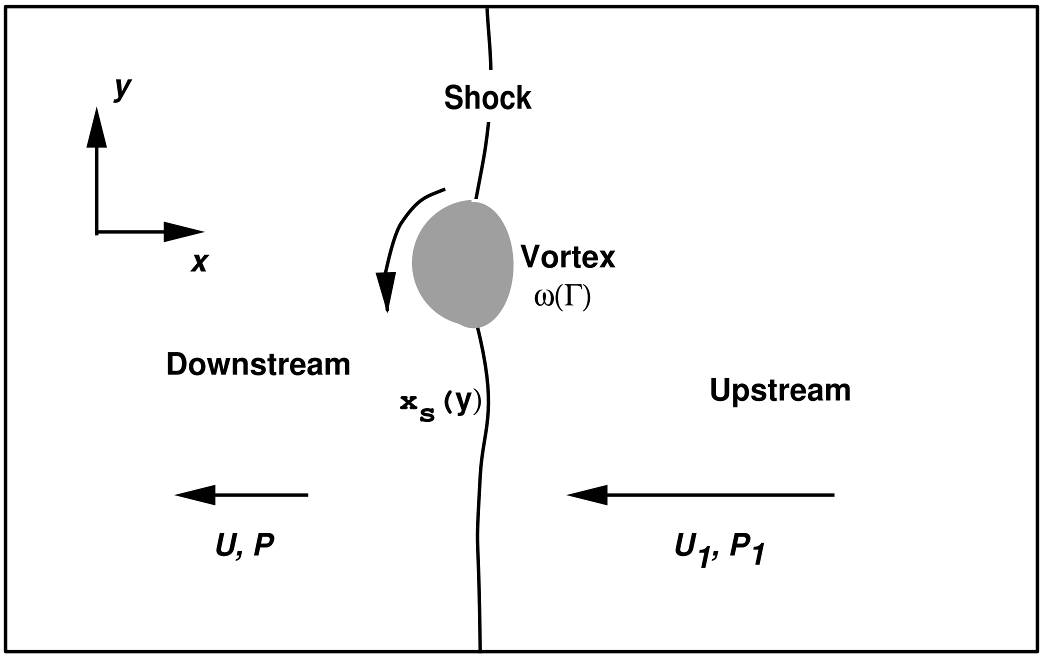

Figure 1: Flow configuration.

In the absence of viscous effects, the shock is infinitesimally thin. Rankine-Hugoniot conditions relate the variables on either side of the shock. However, these conditions are not sufficient to determine the shock velocity uniquely. An additional equation for the shock velocity is therefore derived, which is solved simultaneously with the interior equations (Kopriva, Zang & Hussaini 1991, Canuto *et al.* 1990).

Writing the momentum and pressure equations in the form

$$\begin{aligned} \mathbf{u}_{,t} + \frac{1}{\rho}\nabla p &= -\mathbf{u}\cdot\nabla\mathbf{u} = \mathbf{N}_{\mathbf{u}}, \\ p_{,t} + \gamma p \nabla\cdot\mathbf{u} &= -\mathbf{u}\cdot\nabla p = N_p, \end{aligned} \tag{5}$$

the normal characteristic equation takes the form

$$(p_{,t} - \rho c\,\mathbf{n}\cdot\mathbf{u}_t) + (\rho c\,\nabla\cdot\mathbf{u} - \mathbf{n}\cdot\nabla p)c = N_p - \rho c\,\mathbf{n}\cdot\mathbf{N}_{\mathbf{u}} \tag{6}$$

where $c = (\gamma p/\rho)^{1/2}$ is the sound speed,

$$\mathbf{n} = \left(\frac{1}{(1+x_{s,y}^2)^{1/2}}, \frac{-x_{s,y}}{(1+x_{s,y}^2)^{1/2}}\right) \tag{7}$$

is the unit normal to the shock pointing upstream, and $x_s(y,t)$ is the shock profile. Next, the Rankine-Hugoniot conditions are solved for the downstream velocity and pressure:

$$\delta = \frac{\gamma-1}{\gamma+1}\,\delta_1 + \frac{2\gamma}{\gamma+1}\,\frac{p_1}{\rho_1\delta_1} \tag{8}$$

and

$$p = \frac{2}{\gamma+1}\,\left(\frac{1-\gamma}{2}\,p_1 + \rho_1\delta_1^2\right). \tag{9}$$

In Equations (8)-(9), $\delta = \mathbf{u}\cdot\mathbf{n} - u_s$ and $\delta_1 = \mathbf{u}_1\cdot\mathbf{n} - u_s$, where

$$u_s = w_s\hat{\mathbf{x}}\cdot\mathbf{n} \tag{10}$$

is the shock velocity normal to the shock, while $\hat{\mathbf{x}}$ and w_s are the unit vector in the x direction and the x-component of the shock velocity respectively. We apply Equation (6) at the shock, which requires the time derivatives of p and $\mathbf{u}$. These are obtained directly from (8)-(9):

$$\begin{aligned} \delta_t &= A\delta_{1,t} + Bp_{1,t} + C\rho_{1,t}, \\ p_t &= D\delta_{1,t} + Ep_{1,t} + F\rho_{1,t}, \end{aligned} \tag{11}$$

where

$$\begin{aligned} A &= \frac{\gamma-1}{\gamma+1} - \frac{2\gamma}{\gamma+1}\,\frac{p_1}{\rho_1\delta_1^2}, & B &= \frac{2\gamma}{\gamma+1}\,\frac{1}{\rho_1\delta_1}, \\ C &= -B\,\frac{p_1}{\rho_1}, & D &= \frac{4\rho_1\delta_1}{\gamma+1}, \\ E &= \frac{1-\gamma}{\gamma+1}, & F &= \frac{2\delta_1^2}{\gamma+1}. \end{aligned} \tag{12}$$

Substituting (11) into the characteristic equation (6) gives the evolution equation,

$$(n_x w_s)_{,t} = \frac{(D-\zeta A)(\mathbf{n}\cdot\mathbf{u}_1)_{,t} + \zeta\,(\mathbf{u}\cdot\mathbf{n}_{,t}) + (E-\zeta B)\,p_{1,t} + (F-\zeta C)\,\rho_{1,t} - \mathcal{R}}{D+\zeta(1-A)} \tag{13}$$

for the shock velocity, where

$$\mathcal{R} = N_p - \zeta\,\mathbf{n}\cdot\mathbf{N_u} - \gamma p \nabla\cdot\mathbf{u} - \frac{\zeta}{\rho}\mathbf{n}\cdot\nabla p \tag{14}$$

and $\zeta = \rho c$. Note that Equation (13) is in a general form which is also applicable to three-dimensional and axisymmetric flows. The shock position $x_s(y)$ is the solution of

$$\frac{dx_s(y,t)}{dt} = w_s(y,t) \tag{15}$$

which is solved simultaneously with (13).

3 Numerical Method

3.1 Discretization

For the expediency of fitting the shock, the downstream physical domain, $x_0 \le x \le x_s$, $0 \le y \le y_{max}$, is mapped onto $0 \le X \le 1$, $0 \le Y \le 1$ by the transformation

$$X(x,y,t) = \frac{x-x_0}{x_s(y,t)-x_0}, \tag{16}$$

$$Y(y) = f(y), \tag{17}$$

where x_0 denotes the left physical boundary. The shock is thus defined by $X = 1$. When the flow is periodic in y, $f(y) = y/(2\pi)$. In the non-periodic case,

$$f(y) = \frac{1}{2} + \frac{y}{2}\frac{(1+H^2/y_{max}^2)^{1/2}}{(H^2+y^2)^{1/2}}. \tag{18}$$

The constant H is chosen so that one half the points are contained within $y \in [-y_0, y_0]$ (i.e., $Y \in [.25, .75]$), where y_0 is a user-specified parameter. The relation between H and y_0 is

$$H^2 = \frac{3y_0^2}{1-4y_0^2/y_{max}^2}. \tag{19}$$

The Jacobian of the transformation from physical to computational coordinates is defined by

$$J = \frac{1}{X_x Y_y}. \tag{20}$$

The grid points in physical space have a velocity

$$\mathbf{u}_g = (X\dot{x}_s(y,t), 0). \tag{21}$$

As expected, at the left boundary ($X = 0$), the grid is stationary, while at the shock ($X = 1$), the grid moves with the shock velocity $\dot{x}_s$.

The flow upstream of the shock is fully supersonic, and is not affected by the shock. The only information required by the shock-evolution equation and the downstream Euler equations is the upstream solution at the shock itself. The upstream solution is either known analytically, or can be computed numerically. In either case, it is independent of the downstream solution. For the class of problems wherein the upstream flow is periodic in the streamwise direction, the computational variable in the streamwise direction is then defined by

$$X_1 = \frac{x+\pi}{2\pi}, \qquad\qquad x \in [-\pi, \pi], \tag{22}$$

while $Y_1(y) = Y(y)$. In general, the downstream mesh points along the shock do not coincide with the upstream mesh points, and an interpolation procedure is necessary to transfer information from the upstream domain onto the shock. The interpolation scheme is presented in section 3.2.

When the time-dependent upstream solution is known analytically, the known solution is imposed at the upstream side of the shock prior to imposing the Rankine-Hugoniot conditions. The advantages of the analytical approach are clear: numerical errors due to the upstream solution and interpolation procedure are not present.

All the spatial derivatives in (1)-(4) are first performed in computational space using a 6^{th} order compact discretization. If the spacing between grid points in a particular coordinate direction is h, the derivative $u' = \frac{\partial u}{\partial x}$ at all interior points satisfy the system of equations

$$(u'_{i-1} + u'_{i+1}) + 3u'_i = h^{-1}[(\frac{1}{12}(u_{i+2} - u_{i-2}) + \frac{7}{3}(u_{i+1} - u_{i-1})]. \tag{23}$$

Equations (23) are also applied at the end points in the periodic case. In a non-periodic direction, explicit formulae are used at the first and second end points based on an 8 point stencil. This scheme is referred to as 5^2-6-5^2. The coefficients associated with both periodic and non-periodic stencils are given in Erlebacher, Hussaini & Shu (1996). Derivatives in physical space are obtained by the chain rule using the analytical form of the Jacobian matrix elements (X_x, X_y, Y_x, Y_y) computed from Equations (16)-(17):

$$\begin{aligned}\frac{\partial u}{\partial x} &= \frac{\partial u}{\partial X}X_x + \frac{\partial u}{\partial Y}Y_x,\\ \frac{\partial u}{\partial y} &= \frac{\partial u}{\partial X}X_y + \frac{\partial u}{\partial Y}Y_y.\end{aligned}$$

We now quantify the expected accuracy of the discrete derivative operator applied to $u(x) = \sin(kx)$ as a function of resolution and wavenumber k. Figure 2 shows the error incurred in the derivative calculation with different resolutions by comparing the computed derivative $u'_h(x)$ using the 5^2-6-5^2 stencil, with the analytical result $u'(x)$. The logarithm of the relative error $e = L_2(u' - u'_h)/k$ is plotted versus k in Figure 2a. The L_2 norm of the function $f(x)$ is defined as

$$L_2(f) = \left(\int f^2 \, \mathrm{d}x\right)^{1/2}.$$

For example, on a grid of 96 points, the maximum relative error is 10 percent when $k = 20$. For a grid of 156 points, the relative error for $k = 20$ is 3×10^{-3}, i.e., on the order of 0.3 percent. Several conclusions can be drawn. The most obvious is the deterioration of the derivative error as the resolution per wavelength decreases. In addition, the number of grid points required per wavelength to obtain the correct linear amplitude to within one percent should be greater than 7. This number is determined in the following manner: for a grid size of 96 points, a one percent relative error corresponds to a wavenumber of approximately 14, and $96/14 \approx 7$. This value is essentially independent of the grid size. This is evident from Figure 2b where the relative error is plotted as a function of the number of points per wavelength on four different grids.

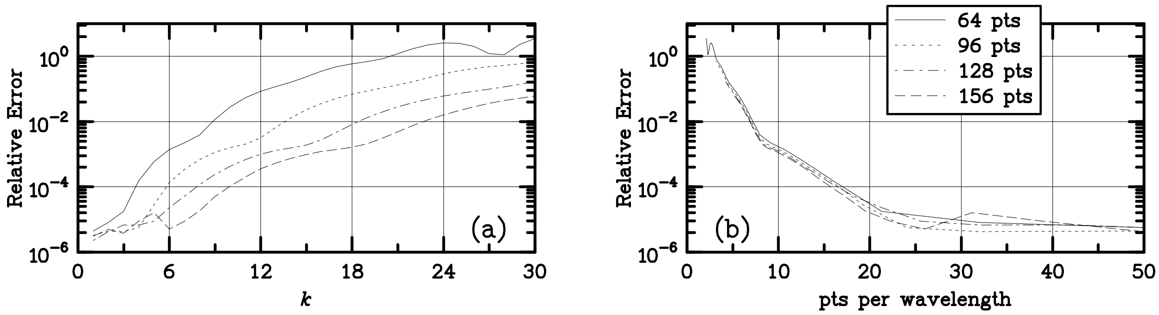

Figure 2: Discretization error for the derivative of $\sin(kx)$. Shown are: (a) the relative errors plotted against the wavenumber k, and (b) the relative errors plotted against the number of points per wavelength, for a sequence of grid resolutions.

Time advancement is based on a low-storage, 5-stage, 4^{th} order accurate Runge-Kutta scheme (Carpenter & Kennedy 1994). Although 5/3 times more expensive than Williamson's 3^{rd} order low-storage scheme at fixed Courant-Friedrichs-Lewy (CFL) number, the achievable CFL number for a linear, constant coefficient, advection equation is higher: 1.67 for the 4^{th} order scheme versus $\sqrt{3}/2$ for the 3^{rd} order scheme. Thus, at the maximum allowable CFL, the new algorithm runs faster per unit of physical time, while providing higher accuracy. The interior equations and shock motion equations are advanced simultaneously in time. The Rankine-Hugoniot conditions are applied at the end of each Runge-Kutta stage to update the downstream variables at the shock.

3.2 Interpolation Scheme

When the upstream solution is computed, it becomes necessary to interpolate the upstream solution along the shock, which does not generally pass through the grid points of the fixed upstream domain. Our experience suggests that when handling high order discretization techniques, it is imperative to maintain a strong degree of consistency between the different components of a numerical algorithm. For example, it is well-known that an algorithm in which gradient and divergence operators are discrete conjugates of each other has better properties than one where both operators are constructed independently. We therefore construct a 5^{th} order interpolation formula consistent with the 6^{th} order interior scheme in the sense that the interpolant is defined by a compact operator (Carpenter, private communication).

Consider a one-dimensional domain $x \in [0, L]$, with N uniformly distributed points $x_i = ih$, $i = 0 \cdots N-1$. We wish to approximate $f(x)$ in the interval $I = [x_i, x_{i+1}]$ by a 5^{th} order polynomial in the variable $y = x - x_{mid}$, where $x_{mid} = (x_i + x_{i+1})/2$. In I, this polynomial takes the form

$$f_h(x) = \sum_{j=0}^{5} a_j \, y^j \tag{24}$$

and has 6 degrees of freedom. Here $f_h(x)$ is the approximation to $f(x)$ in I. The unknown coefficients a_j are chosen to insure that $f(x)$ passes through the points x_{i-1}, x_i, x_{i+1}, x_{i+2}, and is such that its derivative evaluated at x_i and x_{i+1} equals the discrete derivatives f'_i and f'_{i+1} (computed via a compact scheme), respectively. After some algebra, the resulting coefficients are

$$\begin{pmatrix} 128 \;\; a_0 \\ 192h \;\; a_1 \\ 16h^2 a_2 \\ 24h^3 a_3 \\ 8h^4 a_4 \\ 12h^5 a_5 \end{pmatrix} = \begin{pmatrix} 1 & 63 & 63 & 1 & 18h & -18h \\ -1 & -297 & 297 & 1 & -54h & -54h \\ -1 & 1 & 1 & -1 & 10h & -10h \\ 1 & 57 & -57 & -1 & 30h & 30h \\ 1 & -1 & -1 & 1 & 2h & -2h \\ -1 & -9 & 9 & 1 & -6h & -6h \end{pmatrix} \begin{pmatrix} f_{i-1} \\ f_i \\ f_{i+1} \\ f_{i+2} \\ f'_i \\ f'_{i+1} \end{pmatrix}. \tag{25}$$

Note that the coefficients are computed from a stencil of 4 points rather than the 6 points required if only functional values were used. In this sense, the interpolation scheme can be considered to be compact. Using Eq. (25), we can easily transfer information from the upstream domain onto the shock location, assumed to lie within the interval I.

3.3 Downstream outflow boundary

At the subsonic outflow boundary, it is necessary to impose three boundary conditions, one for each characteristic pointing into the physical domain. They are usually implemented by an appropriate set of characteristic boundary conditions. Unfortunately, these conditions usually work well only for weak nonlinearities, and then only when the propagating direction of the disturbances is nearly normal to the boundary. In our simulations however, we are confronted with sound waves that impinge the boundary at all angles, particularly in the case of short domains.

Long time histories, coupled with short domain sizes, suggest the use of a buffer domain approach. A simple strategy, recently developed by Ta'asan & Nark (1995), modifies the governing equations in a finite length "buffer region" adjacent to the outflow boundary. These modifications bend the characteristics in such a way that they all point outwards by the time they hit the downstream boundary. This is achieved by replacing all (computational) time derivatives according to the prescription

$$\frac{\partial}{\partial t} \rightarrow \frac{\partial}{\partial t} + a(X)\frac{\partial}{\partial X}, \tag{26}$$

where $a(X)$ is an artificial velocity field, which is zero outside, and varies smoothly inside, the buffer zone. It is defined in such a way that the acoustic eigenvalues of the modified equations (expressed in computational space)

$$U(0,Y,t) + a(0) \pm c\left[\left(\frac{\partial X}{\partial x}\right)^2 + \left(\frac{\partial X}{\partial y}\right)^2\right]^{1/2}$$

are all positive at the outflow boundary $X = 0$. Here, c is the downstream sound speed and

$$U(X,Y,t) = \frac{\partial X}{\partial t} + u\frac{\partial X}{\partial x} + v\frac{\partial Y}{\partial x} \tag{27}$$

is the contravariant component of the streamwise velocity. The simplest model for $a(X)$ is the power function:

$$a(X) = D\left[1 - \left(\frac{X}{X_b}\right)^b\right], \tag{28}$$

where X_b is the interface between the buffer and the end of the "useful" downstream domain. The constant D is defined as

$$D = 2.5\left(\left[\left(\frac{\partial X}{\partial x}\right)^2 + \left(\frac{\partial X}{\partial y}\right)^2\right]^{1/2} c - |U|\right) \tag{29}$$

evaluated at $X = 0$ when the simulation is initiated. The coefficient of 2.5 is empirical and produces results with little reflection when the width of the buffer domain is at least one characteristic length of the propagating disturbance. A better choice of this coefficient awaits a more rigorous analytical theory which can describe quantitatively the effects of the buffer characteristics on the magnitude of the reflected wave.

The choice of the exponent b is dictated by conflicting requirements. We require that the function $a(X)$ be consistent with the 6^{th} order spatial discretization. However, the larger the value of b, the stronger the variation of $a(X)$ inside a fixed-width buffer. The limit $b \to \infty$ leads to almost total reflection since $a(X)$ then approaches a step function. In practice, we find that $b = 2$ is satisfactory.

4 Linear Theory

In this section, we address the conditions under which the interaction of a linear upstream solenoidal wave with a shock can be reproduced both by linear theory and by numerical simulation. To help resolve issues related to the question of accuracy versus nonlinearity, we constructed a linearized version of the full nonlinear algorithm to allow an unambiguous distinction between linear and nonlinear effects. A linear algorithm produces results independent of upstream amplitude, but retains numerical errors, along with numerical and physical transients. Thus, one can clearly differentiate between these effects and those that are solely the result of nonlinearity. For the sake of numerical consistency, instead of linearizing the Euler equations and discretizing them, we chose to linearize the discretized equations about the undisturbed state.

In the next two subsections, we first consider the interaction of a single plane wave with a shock, and compare the predictions of the algorithm with predictions of linear theory. We then construct a flow field from a superposition of randomly oriented plane waves with a prescribed energy spectrum, and compute the resulting downstream spectrum due to the shock interaction process, and compare it with linear theory.

4.1 Single wave

Consider a single plane vorticity wave of the form

$$\begin{aligned} u - U_1 &= 2\sqrt{2}\epsilon U_1 \frac{k_y}{k}\cos(k_x x + k_y y - U_1 t), \\ v &= -2\sqrt{2}\epsilon U_1 \frac{k_x}{k}\cos(k_x x + k_y y - U_1 t), \end{aligned} \tag{30}$$

$$p = \rho = 1, \tag{31}$$

as conditions in the upstream domain ahead of the shock. Here, $U_1 < 0$ is the nondimensional upstream mean velocity component normal to the undisturbed shock, ϵ measures the intensity of the vorticity wave with respect to the mean flow amplitude, and $k = (k_x^2 + k_y^2)^{1/2}$ is the upstream wavenumber, with $k_y = k\cos\theta$ and $-k_x = k\sin\theta$. The angle between the y axis and the wave vector (measured counterclockwise from the y axis) is denoted by θ, which is also the angle formed between the x axis and the wave front of the incoming vorticity wave. This vorticity wave satisfies the time-dependent linearized Euler equations exactly and represents a wave convecting downstream with constant velocity U_1. For a proper comparison with linear results, and to isolate effects of nonlinear interactions with the shock, we solve the linearized Euler equations upstream of the shock, and the fully nonlinear Euler equations downstream of the shock. Consequently, as ϵ is increased, departures from linear results are limited to the effects of the shock, and not to the processing of upstream nonlinearities by the shock.

Although the upstream wave is an exact solution of the linearized Euler equations, the downstream solution is not known analytically. We solve the linear Euler equations upstream of the shock on a fixed grid and the nonlinear Euler equations downstream of the shock on a moving grid which fits the shock.

Linear theory predicts the presence of three waves in this region: a vorticity wave, an acoustic wave, and an entropy wave (Ribner 1953). The character of the pressure wave depends on the inclination angle θ. For example, if $0° \leq \theta < \theta_{cr}$, the downstream perturbed flow (in a frame of reference in which the flow is steady) is subsonic and the pressure wave shows an exponential attenuation downstream of the shock. If $\theta_{cr} < \theta < 90°$, the downstream flow is supersonic and the pressure wave takes the form of a plane, undamped sinusoidal sound wave. The angle θ_{cr} is referred to as the critical angle (Ribner 1953). Angles less than θ_{cr} are subcritical, while angles greater than θ_{cr} are supercritical. The downstream velocity components are a linear combination of the downstream vorticity wave (whose associated velocity field is solenoidal) and an acoustic wave (whose associated velocity field is irrotational). To isolate the effect of one from the other component, we compute the divergence and vorticity variables. The vorticity wave represents the solenoidal component of the velocity, while the dilatation extracts the irrotational component of the velocity field.

The diagnostics presented below are obtained in the following manner. At each x-station downstream of the shock, consider the periodic profile along $X = const$ (as $\epsilon \to 0$, this curve becomes a straight line parallel to the shock). We Fourier transform the solution in Y, and plot the amplitude of the wave as a function of k_y. Let $f(x_0, y)$ be any variable monitored at a downstream station x. Since k_y is an integer, all variables downstream of the shock are of the general form,

$$f(x, y, t) = \sum_{n=0}^{N_y} A_n(x, t) \cos(ny + \delta_n(x, t)), \tag{32}$$

where $\delta_n(x, t)$ is a phase function, $y \in [0, 2\pi]$, and N_y is the number of points along the shock. If the downstream solution were exactly linear, $A_{k_y}(x, t)$ would be the only nonzero coefficient in (32). However, nonlinearities generate harmonics which generally interact with one another to modify the fundamental ($n = k_y$) mode.

Linear theory results are based on a Fourier decomposition of a time-periodic flow, which leads to Fourier amplitudes and phases which are independent of time. For proper comparison between linear and computed results, it is necessary to insure that initial transients are removed from the system. The transients resulting from an abrupt introduction of upstream disturbances at the shock are greatly reduced by continuously ramping up the disturbance from zero. We choose the ramp-up function

$$f(t^*) = (t^*)^2(3 - 2t^*), \tag{33}$$

where

$$0 < t^* = \frac{t}{Rt_1} < 1 \tag{34}$$

is a nondimensional time, R is the number of periods over which the transient function is active, and

$$t_1 = \frac{2\pi}{k_x|U_1|} \tag{35}$$

measures the time for a single spatial period of the incoming vorticity wave to cross the shock. The ramp-up function is zero at $t^* = 0$ and reaches its maximum value of unity at $t^* = 1$.

Downstream wave amplitudes are related to upstream wave amplitudes via linearly derived "transfer functions" which take different forms in the subcritical and supercritical regions. We compare the amplitudes of velocity $\mathbf{u}$, pressure p, vorticity ω, and dilatation d against linear theory in both the subcritical and supercritical regimes. In all cases, both the upstream and the downstream domains comprise 96^2 grid points, and the buffer domain length is fixed at 30 percent of the downstream domain. The relevant linear transfer functions are given in the appendix as equations (77)-(84). Figures 3-5 show the Fourier amplitudes for u, p, ω and d for the three cases $(-k_x, k_y) = (4, 12), (6, 6), (12, 4)$ at $M_1 = |U_1|\gamma^{-1/2} = 2$ and $\epsilon = 10^{-4}$, respectively. All amplitudes are scaled with respect to their corresponding upstream values. The first case is subcritical with incident angle $\theta = 18.4°$, while the latter two cases are supercritical with incident angles $\theta = 45.0°$ and $\theta = 71.6°$, respectively. The numerical calculations are denoted by the dashed curves and the linear theory by the solid curves. Clearly, the numerical calculations follow precisely the predicted linear value for all x between the buffer domain ($x = 1.25$) and the shock (located at $x = \pi$) for the angles considered. Relative errors on all variables are less than 0.1 percent. For the supercritical case of $\theta = 45°$ (Figure 4), the relative errors on the velocity and the vorticity are on the order of

0.1 percent, while relative errors on the pressure and dilatation waves are on the order of 2-3 percent. The larger errors in the pressure and the dilatation are directly linked to an insufficient number of wavelengths of the downstream pressure wave in the downstream domain. A more complete discussion of this issue is given below. Finally, for the supercritical case of $\theta = 71.6°$ (Figure 5), we see that the relative errors in the pressure and divergence are now on the order of 0.1 percent, while the errors associated with the velocity and vorticity fields are on the order of 2-3 percent. In the latter case, the larger errors are due to insufficient grid resolution. This error magnitude is consistent with Figure 2 which shows larger relative error for higher wavenumbers.

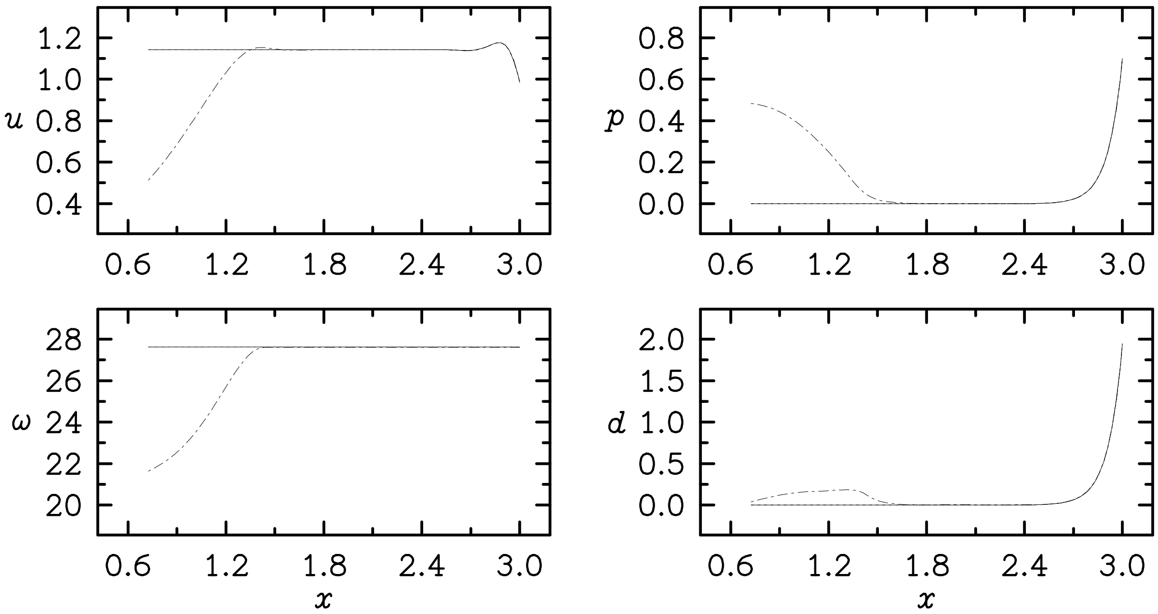

Figure 3: Subcritical case: $k_x = 4$, $k_y = 12$, $\theta = 18.4°$.

For $\theta = 45°$, computed vorticity compares very favorably with linear predictions, while variables related to the acoustic component of the flow less so. The reverse is true at $\theta = 71.6°$. This can be explained in part by considering the variation of k_x'', i.e., the downstream pressure streamwise wavenumber, as a function of the upstream incident angle θ. More precisely, in Figure 6 we plot the variation of

$$\frac{k_x''}{k_x} = -\frac{\tan\theta''}{\tan\theta} \tag{36}$$

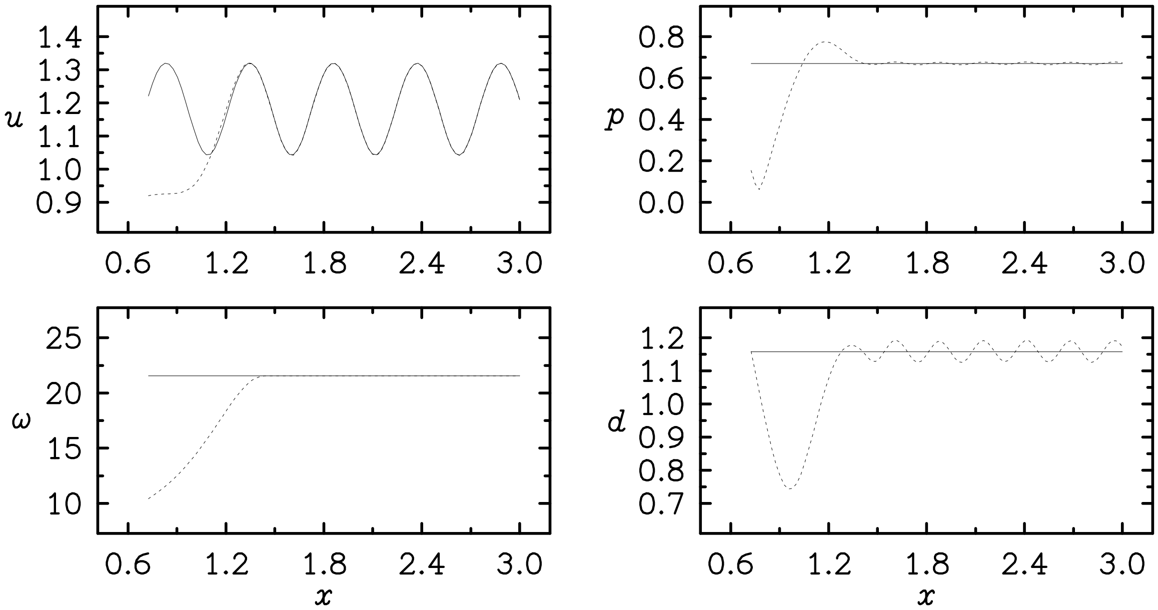

Figure 4: Supercritical case: $k_x = 6$, $k_y = 6$, $\theta = 45.0°$.

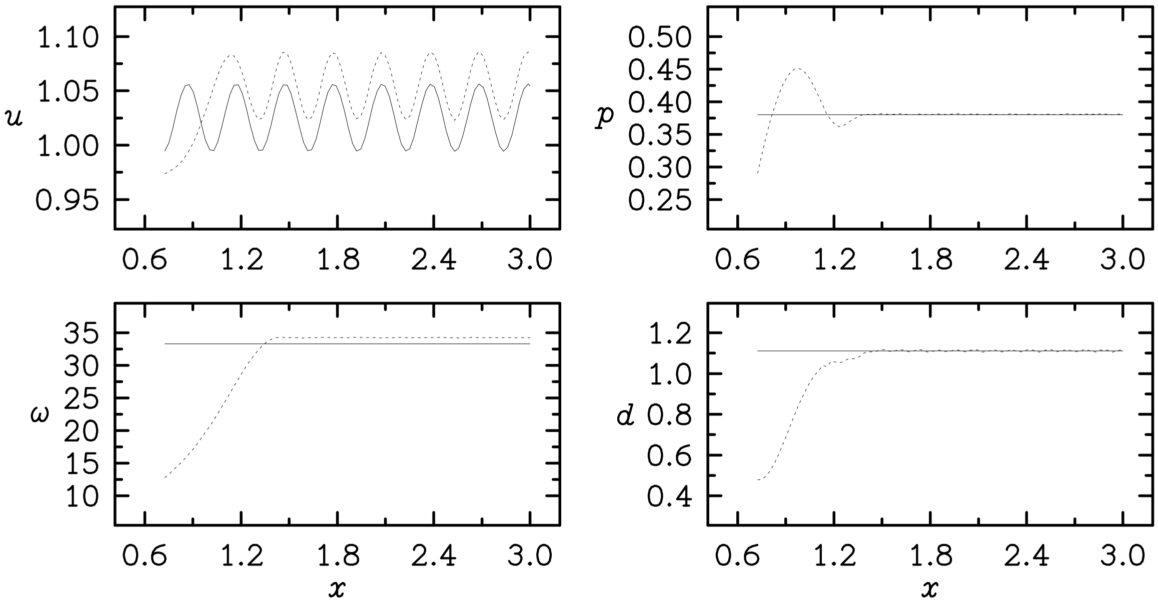

Figure 5: Supercritical case: $k_x = 12$, $k_y = 4$, $\theta = 71.6°$.

as a function of θ over a range of upstream Mach numbers. The streamwise wavenumber k'_x of the downstream vorticity wave is related to k_x via

$$R_1 = \frac{k'_x}{k_x} = \frac{U_1}{U}, \tag{37}$$

which is independent of θ. The relationship between θ'', the angle of the refracted acoustic wave, and θ', the angle of the refracted vorticity wave, is given in the appendix as Eq. (85). Here, U is the normal mean velocity downstream of the shock and is related to U_1 through the mean Rankine-Hugoniot conditions (71)-(73). A detailed derivation of the linear results can be found in Lasseigne *et al.* (1991) which treats the more general case of the linear interaction between a vorticity wave and a shock-induced detonation. The discontinuous slope in Figure 6(a) locates the critical angle θ_{cr}, which decreases and then asymptotes as M_1 increases. For $M_1 = 2$, $R_1 = 2.667$, and $\theta_{cr} = 27.94°$.

To preserve the same number of vorticity waves in both domains, we compress the downstream domain by a factor R_1. That is, at $M_1 = 2$ the downstream grid is defined over the interval $[\pi - 2\pi/R_1, \pi]$. Unfortunately, the wavenumber k_x'' of the pressure wave decreases across the shock for most angles $\theta > \theta_{cr}$; i.e., its spatial scale increases. Even worse, the wavelength of the pressure wave is longer than that of the upstream vorticity wave at some angles. Furthermore, as the Mach number increases, so does the ratio of wavelengths. Consequently, when $k_x = k_y = 6$ ($\theta = 45°$), downstream pressure waves are generated with $k_x'' = 0.23k_x'$. Since the downstream domain contains 6 wavelengths, it only contains 1.4 pressure waves which is insufficient for the buffer domain to absorb properly. The slight wave reflection from the buffer domain generates the oscillations in pressure and dilatation (Figure 4). However, when θ is increased to $71.6°$ and $k_x = 12$, $k_x'' = 0.11k_x'$, the downstream domain contains 12 vortical waves and 4.2 pressure waves. These waves are easily absorbed by the buffer domain whose extent is now more than one pressure wavelength. This is confirmed in Figure 5 by the good agreement in the profiles of dilatation between numerical results and theory.

Figure 7 shows the shear wave inclination angle θ' and pressure wave inclination angle θ'' as a function of θ for several upstream Mach numbers. Note that θ' monotonically increases with θ, while θ'' decreases up to θ_{cr}, and then increases. Thus, the pressure and shear waves travel in opposite y directions for small θ, but as θ increases past θ_{cr}, the direction of the pressure wave reverses until eventually both waves propagate in the same y direction.

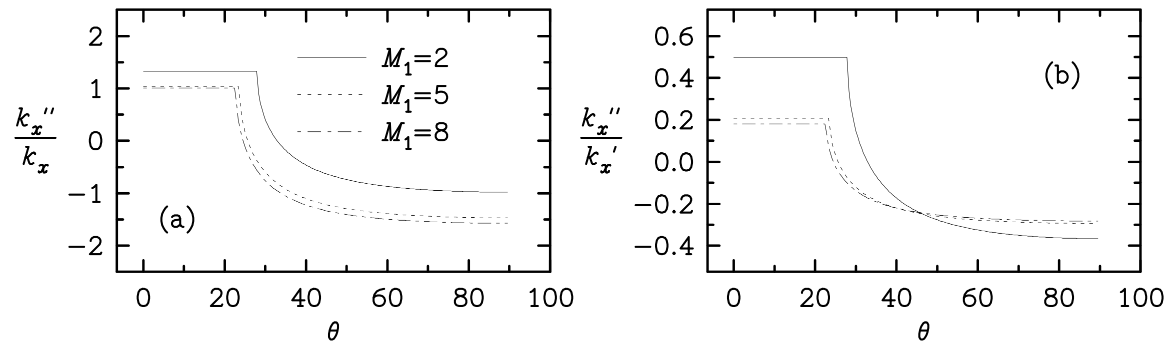

Figure 6: (a) Ratio of downstream pressure streamwise wavenumber k_x'' to the streamwise wavenumber of the incoming vorticity wave k_x as a function of incoming wave orientation θ at upstream Mach numbers of 2, 5 and 8. (b): Ratio of k_x'' to the streamwise wavenumber of the downstream vorticity wave k_x'.

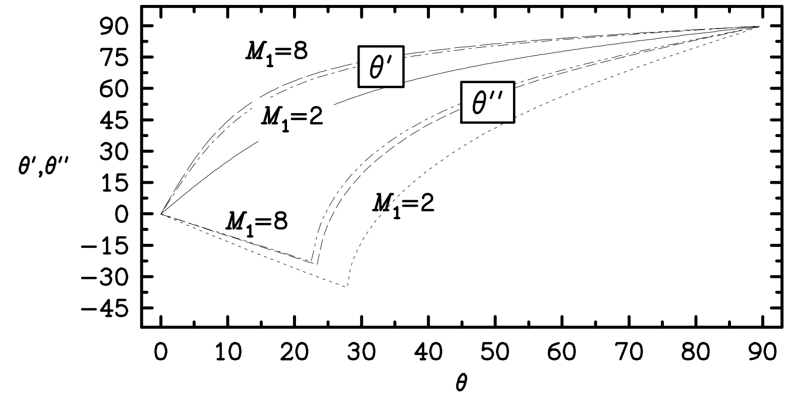

Figure 7: Plots of the shear wave inclination angle θ' and pressure wave inclination angle θ'' as a function of θ for various values of M_1 are shown in Figure 7.

One final comment is in order. Since R_1 is always greater than unity (in fact, $R_1 \in [1, 6)$ for $M_1 \in [1, +\infty)$), the streamwise length scale of a vorticity wave is always compressed downstream of the shock. As a consequence, any flow field constructed from these vorticity waves has its length scales compressed in the direction normal to the shock. This is true in particular for turbulence viewed as a collection of plane vorticity waves. The reduction in the turbulence length scale normal to the shock is in agreement with the numerical studies of Rotman (1991) and Lee, Lele & Moin (1991, 1993), and with the experimental results of Barre (1995). Contrary to the results for vorticity waves, downstream acoustic waves can have wavenumbers (along x) higher or lower than those of the incoming vorticity wave. Thus, streamwise compression does not hold in general for acoustic waves. In the subcritical region, the streamwise length scale of an acoustic wave is always slightly compressed since $k''_x > k_x$ (Figure 6). However, in the supercritical region, angles exist for which $k''_x < k_x$, indicating that the length scale of an acoustic wave can be stretched as well.

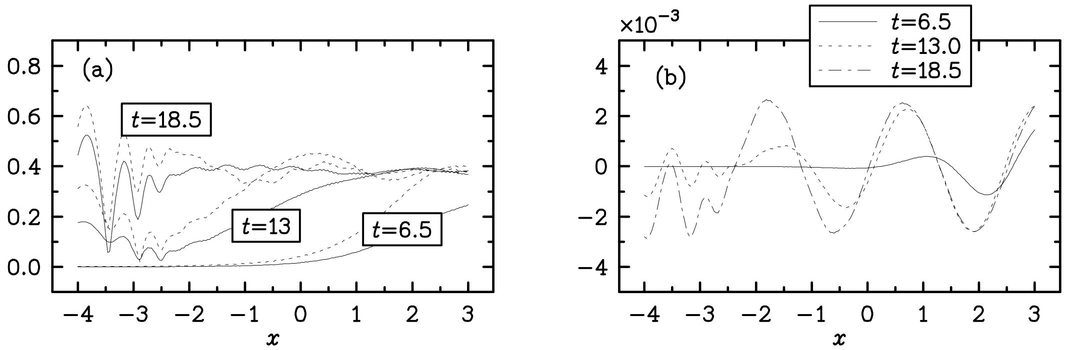

Figure 8: Pressure wave generated from a $\theta = 30°$ upstream vorticity wave at $t = 6.5, 13, 18.5$ for a $M_1 = 2$ shock. (a) Fourier amplitude of pressure, $x_0 = -4$, 25 periods (——), $x_0 = -4$, 15 periods (------); and (b) pressure perturbation, $x_0 = -4$, 25 periods.

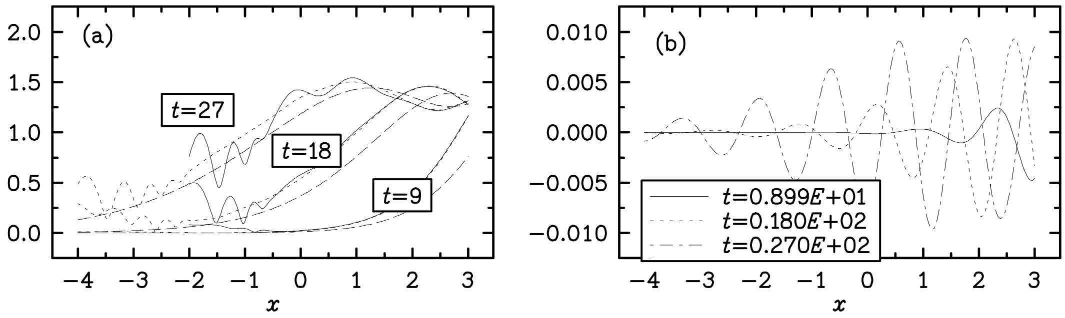

Figure 9: Pressure wave generated from a $\theta = 28.5°$ upstream vorticity wave at $t = 9, 18, 27$ for a $M_1 = 2$ shock. (a) Fourier amplitude of pressure, $x_0 = -12$, 35 periods (– – –), $x_0 = -4$, 25 periods (------), $x_0 = -2$, 25 periods (——); and (b) pressure perturbation, $x_0 = -12$, 35 periods.

The subcritical and supercritical regimes are separated by the critical regime defined by an incident angle close to θ_{cr}, at which point the mean downstream flow is nearly sonic in a frame of reference where the upstream flow is steady. There has been much speculation as to whether the linear theory is still valid in the vicinity of the critical angle. Starting with the work of Zang *et al.* (1984), discrepancies were found between the numerical results and linear theory as the critical angle was approached. The largest errors were on the supercritical side: the flow seemed to become subcritical at a smaller angle than predicted by linear theory. Lasseigne *et al.* (1991) suggested that the apparent discrepancy between linear theory and numerical computations would disappear for angles close to critical if the simulation time were long enough to allow the transients to vanish from the downstream domain. However, the expense of their numerical algorithm prevented extensive checking of this hypothesis. We demonstrate that their hypothesis is correct by considering a vorticity wave impinging a Mach 2 shock at incident angles closer to θ_{cr} than previously simulated. At this Mach number, the critical angle $\theta_{cr} = 27.94°$. Figure 8(a) shows the results at $t = 6.5$, 13, and 18.5 from two different runs at $\theta = 30°$, which is slightly supercritical. The two cases differ by the ramp-up time. Solid lines correspond to a ramp-up time of 25 periods of the upstream wave, while the dashed line has a ramp-up time of 15 periods. Clearly, the longer ramp-up time generates smoother solutions. However, the shorter ramping solution attains the correct mean value at an earlier time. The figure on the right shows the perturbation pressure along $y = 0$ downstream of the shock for a ramp-up time of 25 periods. Clearly, by $t = 18.5$, the solution has converged to its constant amplitude state. In both figures, the effect of the downstream buffer domain (which is 25 percent of the downstream domain) is visible as non-physical oscillations. To show that the time scale over which transient effects vanish from the system increases as $\theta \to \theta_{cr}$, results from three simulations at $\theta = 28.5°$ are shown in Figure 9. In the left figure, results at $t = 9$, 18, and 27 show the wave front moving towards the downstream exit plane at an almost constant velocity. Clearly, a steady state takes much longer to reach than for the previous case. The dashed line serves as a reference curve: the ramp-up time is 35 periods, the downstream boundary is located at $x_0 = -12$, and there are 500 points along x. The streamwise wavenumber is 6. The time taken for one wave period to cross the shock is $t_1 = 0.44$, so the ramping function reaches unity at $t = 15.5$. By $t = 27$, it is clear that the expected oscillatory pattern of the pressure is in the process of establishing itself (Figure 9(b)). We consider two other cases where the ramping time is slightly reduced, with a much shorter physical domain, and with 200 grid points along x (Figure 9(a)). Clearly, the general amplitude of the oscillations is unchanged, but the effect of the buffer domain is clearly visible. These three simulations were performed with the linear numerical algorithm. Our conclusion corroborates that of Lasseigne *et al.* (1991) who stated that the linear results hold up to the critical angle, but the asymptotic solution takes an increasingly long time to reach a steady state. One surmises that there might be an eigenvalue in the time-dependent linear problem, which approaches zero in the limit $\theta \to \theta_{cr}$. We discuss next the possibility of such a zero eigenvalue.

4.1.1 Simple model for zero eigenvalue

Referring to Ribner's paper on the passage of a vorticity wave across a shock (Ribner 1953), we conclude that in a frame of reference in which the flow is steady, $\mathbf{k}''$ is aligned with the downstream mean flow when $\theta = \theta_{cr}$. We denote by ξ the direction of this steady mean flow which is oscillatory in space. At the critical angle, $\theta = \theta_{cr}$, the dynamics of time-dependent perturbations are governed by the one-dimensional Euler equations.

Consider a transient perturbation of the form $e^{i(k_p\xi - \omega t)}$, superimposed on the mean flow, and further suppose that its wavenumber $k_p << k''$. Under this assumption, the wavelength of the perturbation is sufficiently long that it does not sense the underlying steady acoustic wave. Thus, the amplitude of the acoustic wave can be neglected to the lowest order. Inserting the oscillatory perturbation into the Euler equations leads to the dispersion relation

$$\omega_{\pm} = k_p(u_\xi \pm c). \tag{38}$$

The downstream mean velocity u_ξ is the composition of the mean velocity U normal to the mean shock, and the velocity

$$V = -\frac{k_x}{k_y} U_1$$

tangential to the shock. Therefore, the downstream mean velocity along ξ is

$$u_\xi^2 = U^2 + U_1^2 \tan^2\theta.$$

As u_ξ approaches c, θ approaches the critical angle θ_{cr}, and consequently, one frequency goes to zero, while the other corresponds to a wave propagating at a velocity $2c$. One can estimate the rate at which ω_- approaches zero by expanding (38) about the critical angle:

$$\frac{\omega_-}{k_p} = c\tan\theta_{cr}\left[(r^2-1)M^2+1\right](\theta-\theta_{cr}) + O((\theta-\theta_{cr})^2) \tag{39}$$

which clearly demonstrates that as $\theta \to \theta_{cr}$, the time required for the transient waves to wash out of the system increases without bound. Here, r is the ratio of mean densities across the shock.

In order to neglect the transient oscillatory structure of p'', the upstream spatial scale of the transients must be much larger than the downstream wavelength of the pressure wave ($k_x'' >> k_p$). These transients are related to the spatial length scale of the upstream ramping function $f(t^*)$,

$$k_p^{-1} = \frac{f}{f_x} \approx \frac{f}{f_{t^*}} 2\pi R k_x^{-1}. \tag{40}$$

Using $f(t^*) = (t^*)^2(3-2t^*)$, evaluated at $t^* = 0.5$, and the knowledge that k_x'' is on the same order as k_x (see Figure 6), one finds that the transients effects on p'' can be safely neglected if $R >> 1$, which is clearly satisfied in our numerical experiments ($R > 10$).

The main assumption of this analysis is that the spatial scale of the transients is sufficiently large with respect to that of the downstream acoustic wave. However, this might not always be the case. A Floquet analysis of the one-dimensional Euler equations may then be necessary.

4.2 Random collection of waves

After analyzing the passage of a single vorticity wave through a shock, we progress to a somewhat more realistic representation of turbulence. In this description, a random collection of vorticity waves is convected through the shock. When the amplitudes of the waves are sufficiently small, linear theory applies, and the spectrum downstream of the shock can be derived analytically by Fourier decomposition. Ribner (1987) and Jackson *et al.* (1991) used this approach to derive analytically the downstream spectra of "turbulence" convecting through a shock. By considering each wave individually, the downstream spectrum was determined by superposition of the individual downstream waves.

In this section, we consider a range of sufficiently large amplitudes of the upstream disturbances to determine the effects of nonlinear interactions. Now, it is no longer possible to consider the passage of each wave individually, but we must instead consider the flow field as a whole. First, we construct the upstream velocity field by superposition of individual plane waves. Second, we convect this flow field through the shock, and finally, we Fourier decompose the downstream quantities along the shock to determine their one-dimensional spectrum.

To quantify the range of parameters for which the linear theory is a valid approximation, we also compute the downstream spectrum as explained in Ribner (1987). To compare linear and nonlinear results, we compute the spectrum of individual flow variables in the direction parallel to the shock.

Consider the power spectral density $[uu]$ for an isotropic upstream state:

$$< u^2 >= \int_{-\infty}^{\infty} \int_{-\infty}^{\infty} [uu] \, \mathrm{d}k_x \, \mathrm{d}k_y = \int_{-\infty}^{\infty} E(k) \mathrm{d}k \tag{41}$$

where $E(k)$ is the two-dimensional energy spectrum of the upstream streamwise velocity fluctuations u. Each wave in this spectrum is processed by the shock, and thus generates a spectrum downstream of the shock which is no longer isotropic. The downstream flow properties depend on x and therefore we consider the effect of the shock on the lateral spectrum

$$E(k_y) = \int_{-\infty}^{\infty} [uu] \, dk_x. \tag{42}$$

Since the isotropic spectrum is a function of the wavenumber magnitude $k = (k_x^2 + k_y^2)^{1/2}$, it is convenient to change the integration variable in (42) from k_x to k:

$$E(k_y) = 2 \int_{k_y}^{\infty} \frac{[uu]}{(k^2 - k_y^2)^{1/2}} \, k \, \mathrm{d}k. \tag{43}$$

The downstream lateral spectrum is now easily obtained by considering that a downstream variable $\mathcal{V}$ is related to an upstream variable via $\mathcal{V} = \Gamma_{\mathcal{V}} u$ where $\Gamma_{\mathcal{V}}$ is the linear transfer function:

$$E_{\mathcal{V}}(k_y) = 2\int_{k_y}^{\infty} \frac{\Gamma_{\mathcal{V}}^2[uu]}{(k^2 - k_y^2)^{1/2}}\, k\mathrm{d}k. \tag{44}$$

We compute both numerically and theoretically the spectra of ρ, p, u, and v, where u and v are the longitudinal and tangential velocity components, respectively (Jackson *et al.* 1991). In addition to the usual variables, we focus particularly on the vorticity ω and the dilatation d since they best represent vortical motion, and compressibility effects respectively. Precise definitions of all transfer functions are given in the appendix.

The spectrum under consideration is similar to the initial spectrum in homogeneous incompressible turbulent flow simulations,

$$E(k) = k^4 e^{-2k^2/k_0^2}, \tag{45}$$

which leads to

$$[uu] = \frac{32}{3(2\pi)^{1/2}} \left(\frac{k}{k_0}\right)^2 k_0^{-2}\, \overline{u^2}. \tag{46}$$

Equation (43) is evaluated by numerical integration with a sufficient number of points to ensure accurate results. The same energy spectrum is prescribed initially for u and v. The upstream conditions are

$$\begin{aligned} u(x,y) &= U_1 + \epsilon\sqrt{2}u_1'(x,y), \\ v(x,y) &= \epsilon\sqrt{2}v_1'(x,y), \end{aligned} \tag{47}$$

$\rho = p = 1$, while ϵ measures the intensity of the input turbulence. The perturbation velocity field is a random field with a two-dimensional energy spectrum given by (45) and with rms ϵU_1.

We perform simulations at $\epsilon = 0.001$ and $\epsilon = 0.01$ and compare the results with those from linear theory and linear simulations. Figure (10) plots theoretical results as a solid line and linear numerical results as a dashed line. This figure displays the numerical results for the vorticity and dilatation as a function of the wavenumber k_y for amplitudes of $\epsilon = 0.01$

and 0.001 on a 96×96 downstream grid. The spectra are computed immediately downstream of the shock, and are not averaged in time. Note that the curves from linear theory and linear simulations are almost indistinguishable from each other over eight decades.

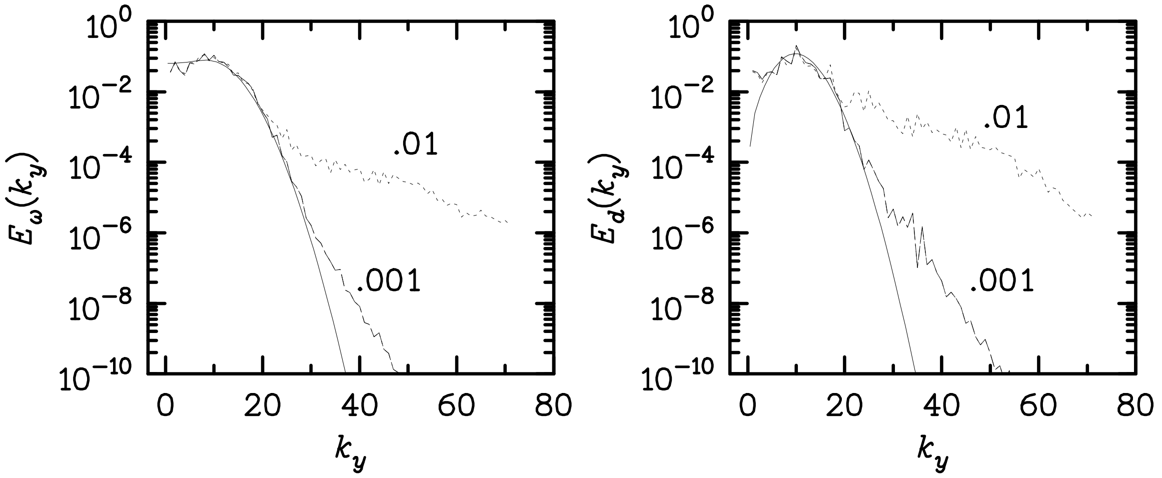

Figure 10: Spectra of the vorticity and dilatation as a function of k_y for input turbulence intensities of $\epsilon = 0.01$ and 0.001. The solid line represents linear theory, and the dashed line the computations based on linear algorithm. Note that these two are essentially indistinguishable.

Nonlinearities leave the large scale (small wavenumbers) component of the spectrum unchanged and increase the energy in the smaller scales (large wavenumbers). The unaffected range of scales decreases with increasing turbulent intensity. Nonlinearities arise from two sources – shock interaction, and the quadratic terms in the downstream governing equations. As an initial approximation, nonlinear effects at wavenumber k become noticeable when the quadratic interactions at wavenumber $k/2$ produce waves of the same amplitude as those found linearly at wavenumber k. This can be expressed as

$$\epsilon^4 E(k_y/2)^2 = \epsilon^2 E(k_y). \tag{48}$$

If the energy spectrum is of the form (45), then the relation (48) predicts that k/k_0 increases with decreasing ϵ. In the limit of $\epsilon \to 0$, there are no nonlinear effects.

To address the issue of grid resolution, we show in Figure 11 the spectrum of the dilatation for two different grid sizes and at two different input turbulent intensities. In this figure, the dashed curve corresponds to a 96^2 grid, while the solid curve corresponds to a 156^2 grid.

There is close agreement between the two curves. Therefore, the deviation of results for $\epsilon = 0.01$ from those at $\epsilon = 0.001$ is clearly due to nonlinear effects.

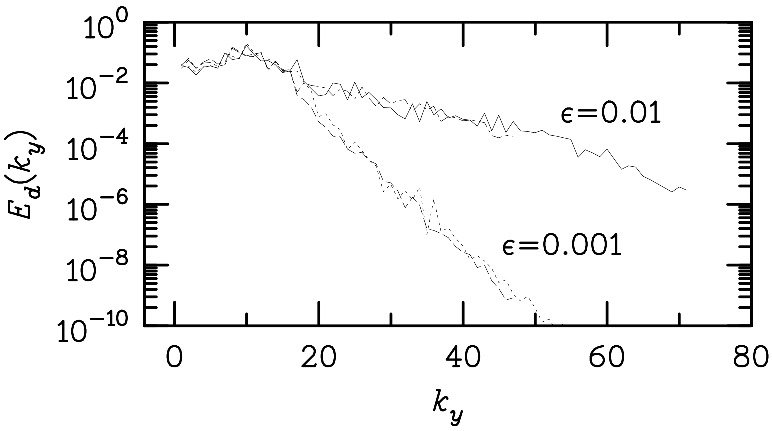

Figure 11: Comparison of dilatation spectra for two different grid sizes and at two different input turbulent intensities.

5 Shock-Vortex Interaction

Although there have been many numerical and experimental studies of a vortex interacting with a shock, there have been few, if any, quantitative studies of the nonlinear interaction processes. In fact, to the authors' knowledge, there are no theoretical studies which address the nonlinear effects when the vortex axis is parallel to the shock. In this section, we discuss the results of a systematic study, based on the numerical solution of the fully nonlinear Euler equations, of the interaction of an initially plane shock with a homentropic Burger vortex. Specifically, the azimuthal velocity and density of the vortex are given by

$$v_{\theta 1} = \frac{\Gamma\, r}{2\pi {r_0}^2}\, e^{0.5(1-r/r_0)^2}, \tag{49}$$

$$\rho = T^{1/(\gamma-1)}, \tag{50}$$

where

$$T = T_1 - \frac{(\gamma-1)\Gamma^2}{8\gamma\pi^2 {r_0}^2}\, e^{1-(r/r_0)^2}. \tag{51}$$

The vortex has a circulation Γ and a core radius $r_0 = 0.3$. It is initially centered at $x = 4.5$ and convects with velocity U_1 towards the shock which is situated at $x = \pi$. The vortex center intersects the shock at $t = (4.5 - \pi)/|U_1|$, which leads to the convenient definition of a nondimensional time variable,

$$t^* = \frac{|U_1|t - (4.5 - \pi)}{r_0}. \tag{52}$$

With this change of time variable, the vortex center intersects the undisturbed shock at $t^* = 0$, while the vortex core boundaries cross the mean shock location at $t^* = \pm 1$.

Downstream of the shock, the fast acoustic wave, which propagates at a velocity $|U| + c$, reaches the buffer boundary at

$$t_b^* = \frac{U_1}{U} \frac{L_p/r_0}{1 + 1/M}, \tag{53}$$

where L_p is the length of the downstream domain excluding the buffer region. The downstream boundary is at $x = -1$, and the length of the buffer domain is ten percent of the downstream extent. All time histories extend from $t^* = -3$ to $t^* = 15$. For the chosen parameters, t_b^* varies from 12.1 at Mach 2 to 19.5 at Mach 8.

The upstream domain is defined by $0 \leq x \leq 2\pi$ and $-10 \leq y \leq 10$. Although we know the analytical solution, the linear advection equation is nonetheless solved numerically with a sixth order method for consistency.

To quantify the effect of M_1 and Γ on the structure of the downstream flow, we monitor the mean square quantities such as mean square velocity, KE $=< u^2(t) > / < u_1^2(0) >$, the mean square pressure, PE $=< p^2(t) > / < u_1^2(0) >$, the mean square vorticity (enstrophy), ENS $=< \omega^2(t) > / < \omega_1^2(0) >$, and the mean square dilatation, DIL $=< d^2(t) > / < \omega_1^2(0) >$. Angular brackets denote integration over the upstream or downstream domain according to the argument.

Results from computations at $M_1 = 2$ and 8 are shown in Figures 12 and 13, respectively. At each Mach number, we consider several values of circulation Γ. As Γ increases from 0.03 to 1, nonlinear effects become evident. They appear in these figures as departures from the time history at $\Gamma = 0.03$ which serves as a linear reference curve.

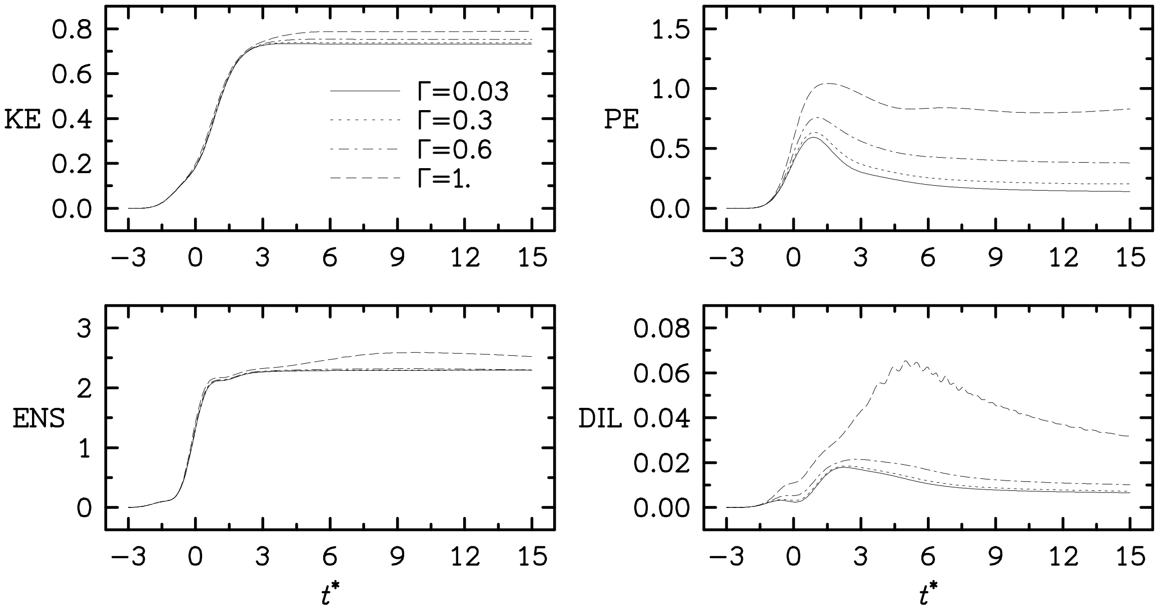

Figure 12: Time history of mean square velocity (KE), pressure (PE), enstrophy (ENS) and dilatation (DIL), for a $M_1 = 2$ shock.

It is to be noted that enstrophy is least affected by nonlinearities at both low and high Mach numbers. At $M_1 = 2$, nonlinear effects are negligible for $\Gamma \leq 0.6$. Departures from linearity are already evident at the higher Mach number and are already noticeable at the next to lowest computed circulation. In a later section, a high Mach number expansion of the linearized Rankine-Hugoniot relations will show that nonlinearities become important when $\Gamma = O(1/M_1)$.

The stronger nonlinearities in the time histories of mean square velocity suggest that they are due to the irrotational component of the velocity field. This is confirmed by examining the time histories of dilatation and mean square pressure. Contributions to the latter come from two sources:

1. from the $O(\Gamma)$ pressure field of the acoustic wave generated through the interaction of the shock with the vorticity field,

2. from the $O(\Gamma^2)$ pressure field associated with the downstream vortex.

The plots of mean square dilatation are consistent with the above observations. Since the

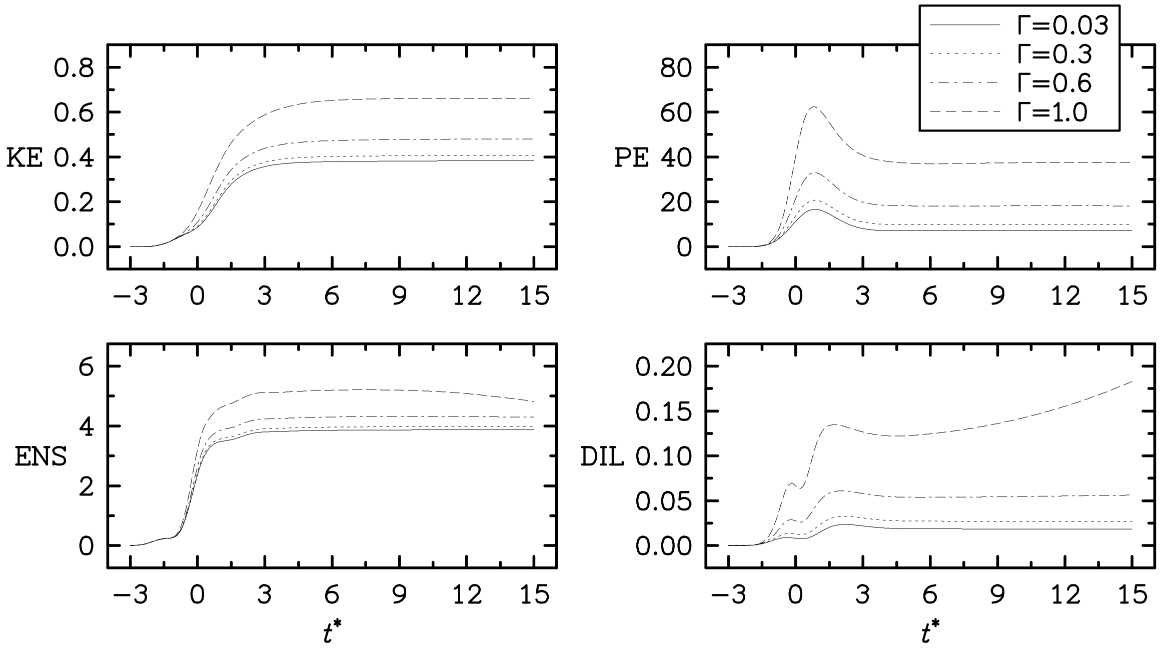

Figure 13: Time history of mean square velocity (KE), pressure (PE), enstrophy (ENS) and dilatation (DIL), for a $M_1 = 8$ shock.

downstream vorticity produces very little dilatation, and since to lowest order, mean square dilatation is $O(\Gamma^2)$ (see Equations (65)-(66)), the time history of dilatation at $M_1 = 2$ shows only moderate quadratic scaling. There is an anomaly at $\Gamma = 1$, evidenced by much stronger amplitudes of mean square dilatation, along with some numerical oscillations. A two-dimensional plot of pressure perturbation (Figure 21) suggests the presence of a triple point along the shock which accounts for the numerical oscillations. At the higher Mach number, there is quadratic scaling for $\Gamma > 0.3$ when $t^* < 2$. However, we notice a strong increase of mean square dilatation for $\Gamma = 1$ when $t^* > 5$, which is indicative of a physical process not present at the lower circulation levels, perhaps due to the steepening of the pressure front in the acoustic pulse (Figure 22).

The interplay between the pressure field associated with the vortex (hereafter referred to as core pressure) and the acoustic pulse (acoustic field associated with the irrotational component of the velocity field) can perhaps best be seen from the time history of the dilatational energy. As the vortex crosses the shock, mean square pressure initially increases

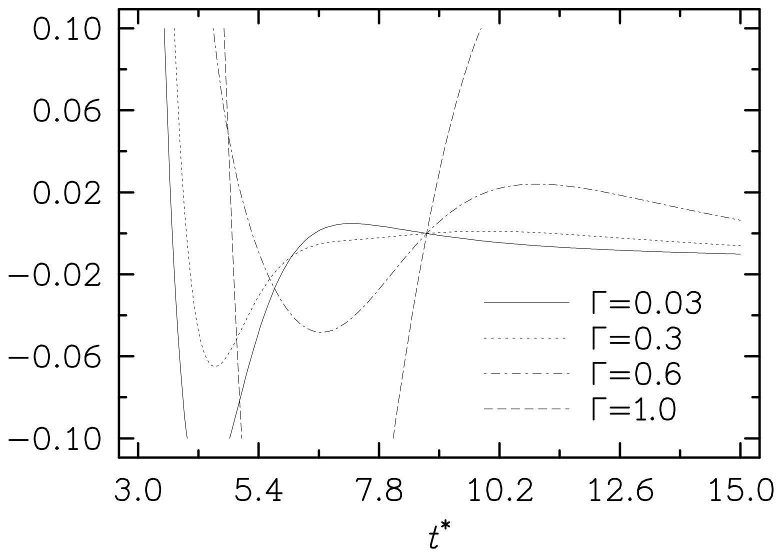

Figure 14: Time history of PE(t^*)-PE(1)=1 for $\Gamma = 0.03$, 0.3, 0.6 and 1. $M_1 = 8$.

from zero to a maximum value at around $t^* \approx 1$. Once the maximum is reached, there are two distinct time ranges. The first, which extends from $t^* = 1$ to $t^* = 3.3$, shows a sharp decay rate of mean square dilatation and mean square pressure corresponding to the separation of the circular acoustic pulse from the vortex core. Mean square pressure reaches a minimum shortly beyond $t^* = 1$, rises, and then decays very slowly. This is shown in Figure 14 which plots PE(t^*)-PE(1) for the lowest four circulations. From Figure 13, it appears that the mean square pressure at $M_1 = 8$ is constant once $t^* > 3.3$, but as seen in Figure 14 the mean square pressure is actually decaying.

In the following sections, we examine more closely the time history of the dominant terms in the transport equations of mean square pressure, enstrophy, and dilatation.

Enstrophy

The evolution equation for $< \omega^2 >$ is

$$\begin{aligned} \frac{\partial}{\partial t} < \omega^2 > &= - < \omega^2 d > +2 < (\nabla p \times \nabla \rho^{-1}) \cdot \vec{\omega} > \\ &+ < \omega^2 \nabla \cdot \mathbf{u}_g > - < (\mathbf{u} \cdot \mathbf{n}) \omega^2 >_S, \end{aligned} \tag{54}$$

where $< >$ denotes integration over the entire downstream domain and $< >_S$ refers to integration along the shock. In the above equation, $\mathbf{u}_g$ is the grid velocity (21) which

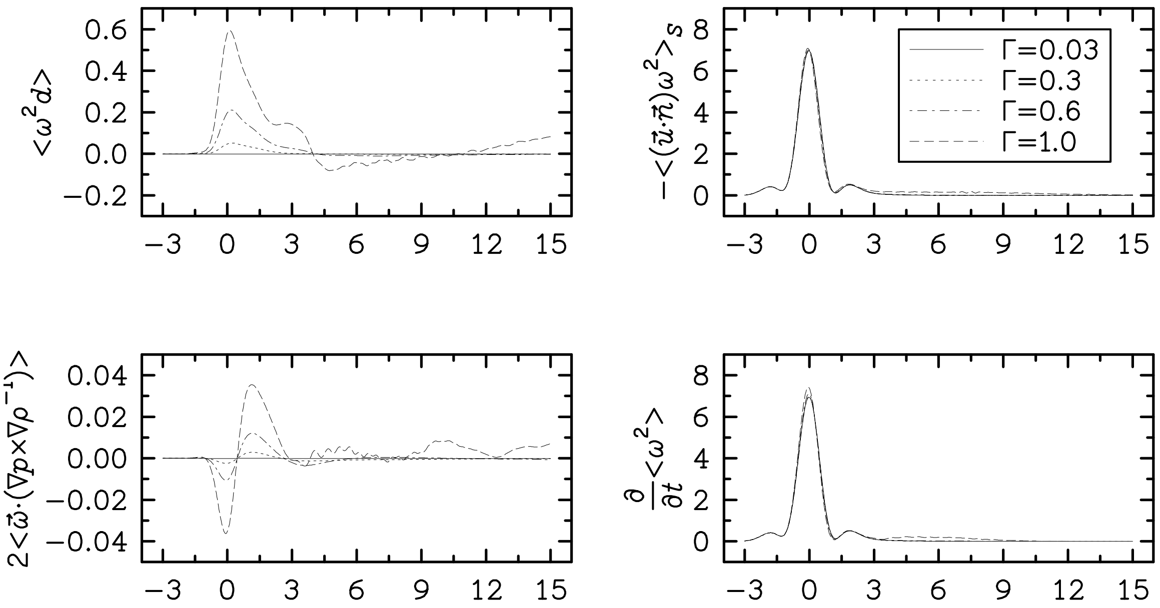

Figure 15: Enstrophy budget at $M_1 = 2$. The ordinates are normalized by $< \omega_1^2(0) >$.

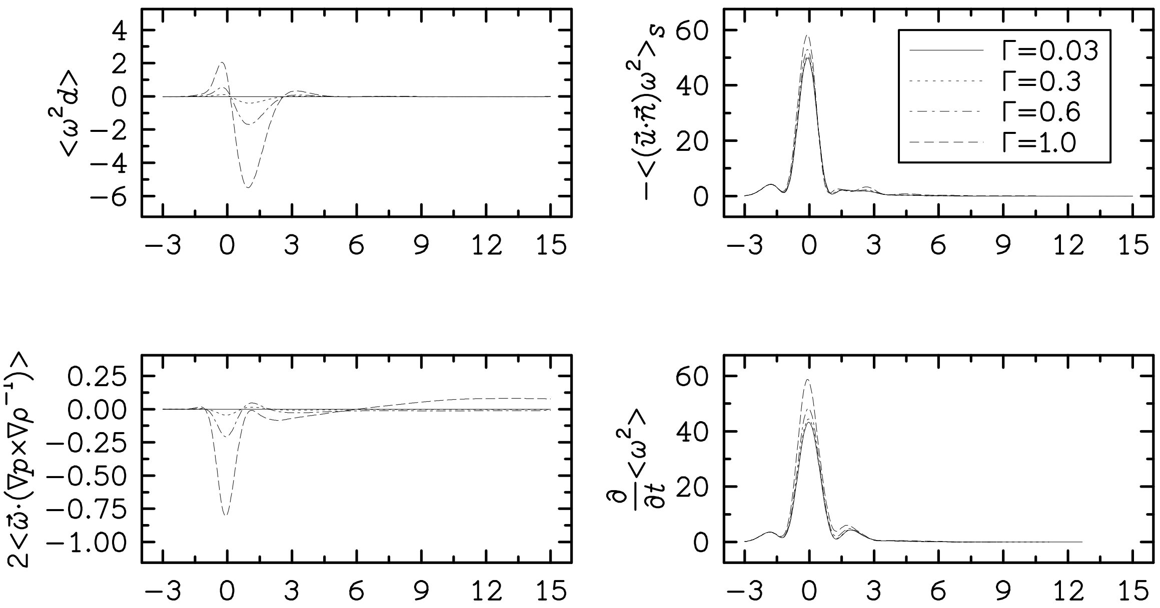

Figure 16: Enstrophy budgets at $M = 8$. The ordinates are normalized by $< \omega_1^2(0) >$.

results from the shock-fitted coordinate system. The successive terms on the right hand side of Equation (54) represent the generation of vorticity due to convective effects (term I), baroclinic torque (II), shock motion (III), and the instantaneous shock interaction (IV). Term (IV) is positive; this indicates that the shock is always a source of vorticity. The sign

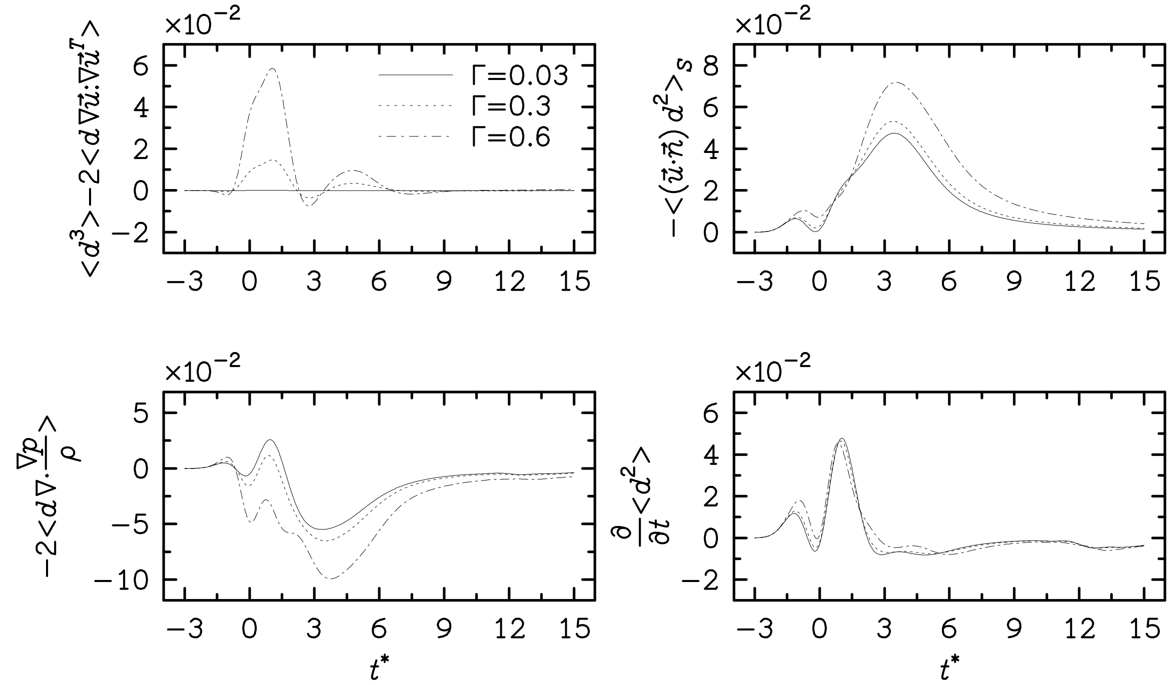

Figure 17: Dilatation budget at $M_1 = 2$. The ordinates are normalized by $< \omega_1^2(0) >$.

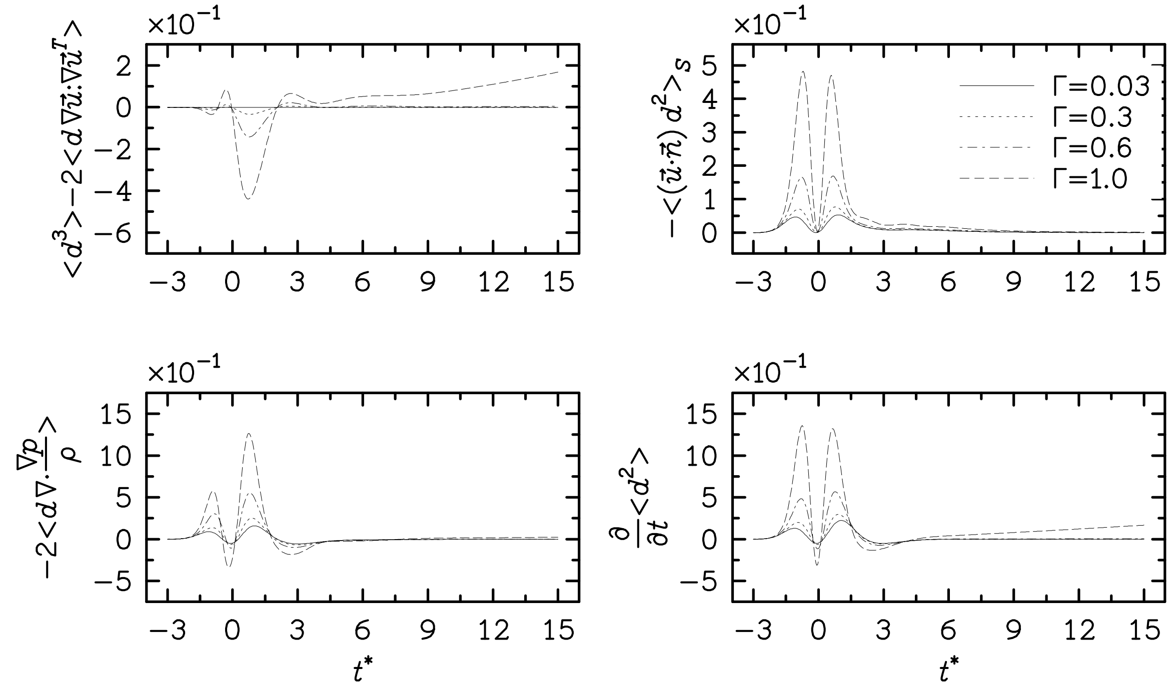

Figure 18: Dilatation budget at $M_1 = 8$. The ordinates are normalized by $< \omega_1^2(0) >$.

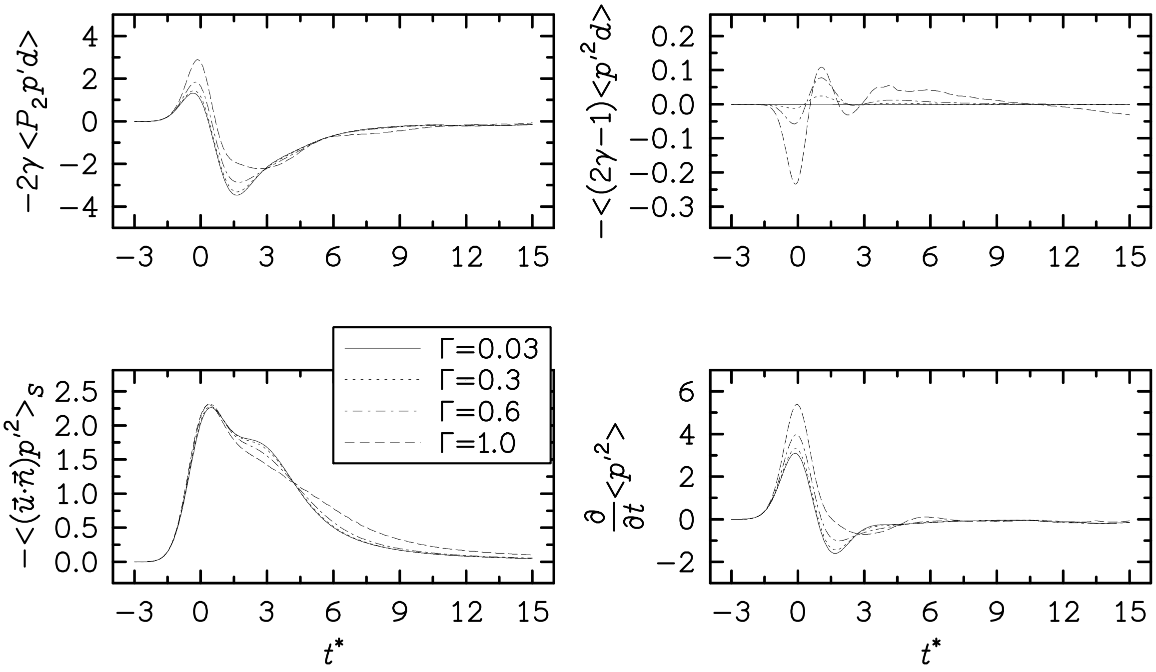

Figure 19: Pressure budget at $M_1 = 2$. The ordinates are normalized by $< u_1^2(0) >$.

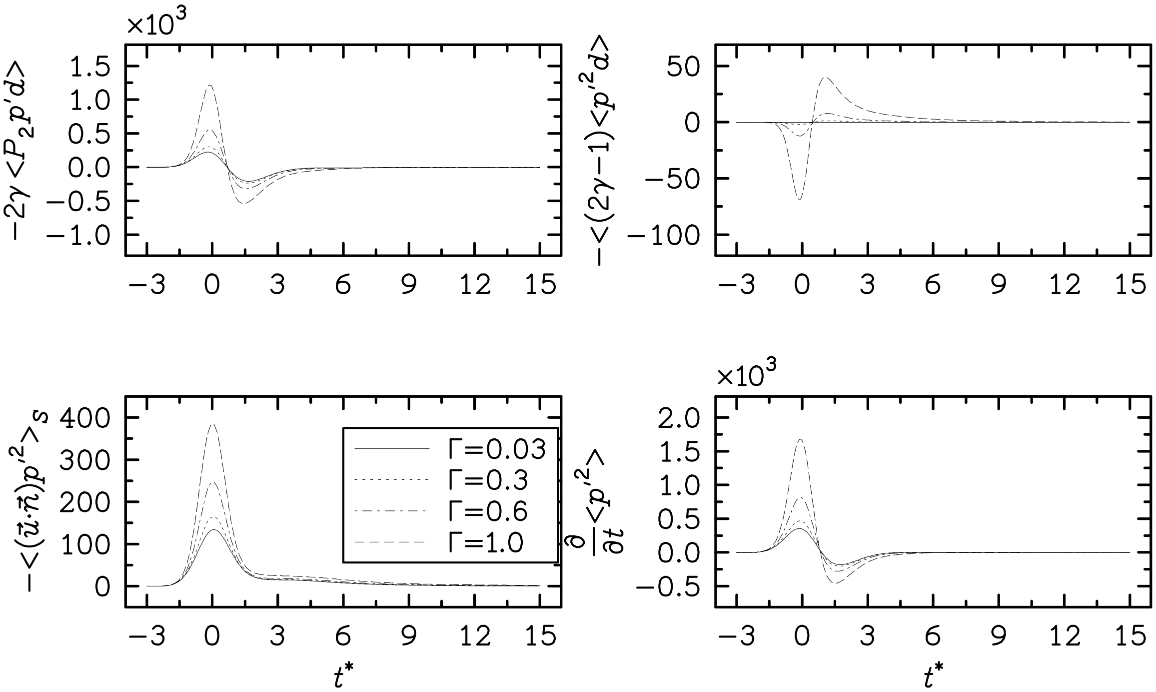

Figure 20: Pressure budget at $M_1 = 8$. The ordinates are normalized by $< u_1^2(0) >$.

of term (II) is a measure of non-barotropic effects behind the shock, which can be neglected.

Dilatation

The mean square dilatation in the downstream domain satisfies

$$\begin{aligned} \frac{\partial}{\partial t} < d^2 > &= + < d^3 > -2 < d \, \nabla \mathbf{u} : \nabla \mathbf{u}^T > \\ &- 2 < \nabla \cdot \left(\frac{\nabla p}{\rho} \right) d > + < d^2 \nabla \cdot \mathbf{u}_g > - < (\mathbf{u} \cdot \mathbf{n}) \, d^2 >_S . \end{aligned} \tag{55}$$

The rate of change of mean square dilatation is the result of convective effects (I & II), pressure gradient effects (III), shock motion (IV), and the instantaneous shock interaction (V). The shock acts as a source of dilatation. All terms (with the exception of IV) have the same order of magnitude (Figure 17 and 18).

Pressure

Let $p' = p - P$ denote the perturbation pressure whose mean square satisfies

$$\begin{aligned} \frac{\partial}{\partial t} < p'^2 > &= -2\gamma < P \, p' d > -(2\gamma - 1) < p'^2 d > \\ &+ < p'^2 \nabla \cdot \mathbf{u}_g > - < (\mathbf{u} \cdot \mathbf{n}) \, p'^2 >_S . \end{aligned} \tag{56}$$

The various contributions to the rate of change of mean square pressure are convective effects (I-II), which include pressure-dilatation correlations, shock motion effects (III), and the instantaneous shock-interaction effect.

The time history of the dominant terms in the budgets of these three quantities as a function of the circulation at Mach 2 and Mach 8 are presented in Figures 15-20. The direct interaction of the shock with the upstream vortex (term IV) in Equation (56) dominates the production of enstrophy until $t^* = 1$ at both Mach numbers. During this period, the baroclinic torque contributes less than one percent to enstrophy, while $< \omega^2 d >$ contributes on the order of ten percent. However, the time histories of the baroclinic and $< \omega^2 d >$ terms change character significantly as the Mach number increases from 2 to 8. For example, whereas the minimum and maximum of (II) are approximately balanced at $M_1 = 2$, the negative component is much stronger than the positive one at $M_1 = 8$. This is directly related to the strong quadratic amplification of the upstream pressure field at high M_1 and high Γ.

Figures 17-18 show time histories of the dominant terms in the evolution of the mean square dilatation, $< d^2 >$. At the lower Mach number, there are strong contributions of $< d\nabla \cdot (\nabla p/\rho) >$ and $< (\mathbf{u} \cdot \mathbf{n})d^2 >$ past $t^* = 3$, but the two terms almost cancel out each other as evidenced by the evolution of $< d^2 >_{,t}$ in Figure 17. This cancelation results from the near absence of a solenoidal pressure component in the dilatational field. At Mach 8, the convective and thermodynamic terms (I-III) have amplitudes up to 20 times larger than those at $M_1 = 2$. The primary reason is that at high Mach number, the resulting downstream acoustic field scales quadratically with M_1. Thus, the contributions to the dilatation from the upstream velocity field (which are linear in Γ) are no longer visible on the scale of the figure. As a consequence, the generation of dilatation at the shock and its time-rate of change, $< d^2 >_{,t}$ appear to be symmetric in time about $t^* = 0$. In the absence of an upstream velocity field, the symmetry in time is exact.

The time variation of $< p'^2 >$ is similar at both Mach numbers, except for stronger nonlinearities at $M_1 = 8$ (Figures 12-13). The dominant terms of the perturbation pressure energy budget, normalized by $< u_1^2(0) >$ are shown in Figures 19-20 for $M_1 = 2$ and 8, respectively. Only two terms play a significant role in Eq. (56): the mean pressure dilatation term (I), and the production term at the shock (IV). The latter term is linear at $M_1 = 2$ up until $t^* = 1$ when the trailing vortex edge crosses the shock, at which point moderate nonlinear effects take place for $\Gamma \geq 0.6$. Nonlinear interactions decrease the production of mean square pressure $< p'^2 >$ until $t^* = 4.5$. At $M_1 = 8$, its production at the shock is highly nonlinear, starting from $\Gamma = 0.3$. This nonlinearity is most easily seen by comparing the difference between successive curves with the $\Gamma = 0.03$ curve, which is representative of linear theory. At both Mach numbers, this term decreases strongly until $t^* = 1$, followed by a sudden decrease in the decay rate once the downstream vortex has cleared the shock. However, at the lower M_1 and the lower circulations, the sharp decay resumes once $t^* = 3$.

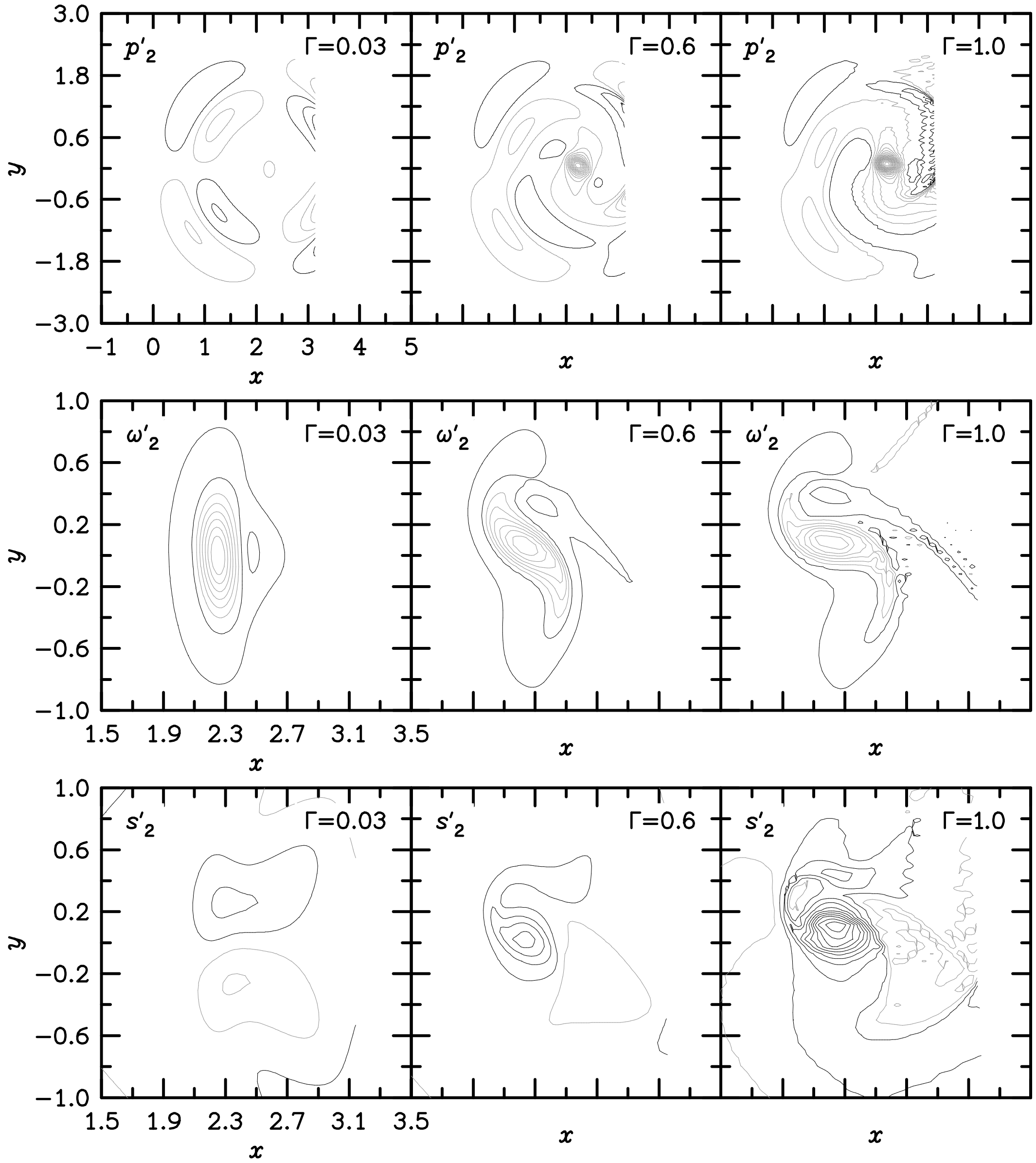

Figure 21: Contour plots of pressure (top row), vorticity (middle row) and perturbation entropy $(\log((p/P)/(\rho/\rho_0)^\gamma))$ (bottom row) at $\Gamma = 0.03$ (left column), 0.6 (middle column) and 1.0 (right column). $M_1 = 2$. The axis labels are the same across rows.

This does not occur at $M_1 = 8$.

To visualize the effect of nonlinearity on the pressure pulse and on the vortex core structure, we plot contours of pressure, vorticity, and entropy at $\Gamma = 0.03$, 0.6 and 1.0 at $M_1 = 2$ and 8 in Figures 21-22. All three variables are normalized by Γ. The contour values have the same range for all circulations, for consistent comparison, except for the perturbation

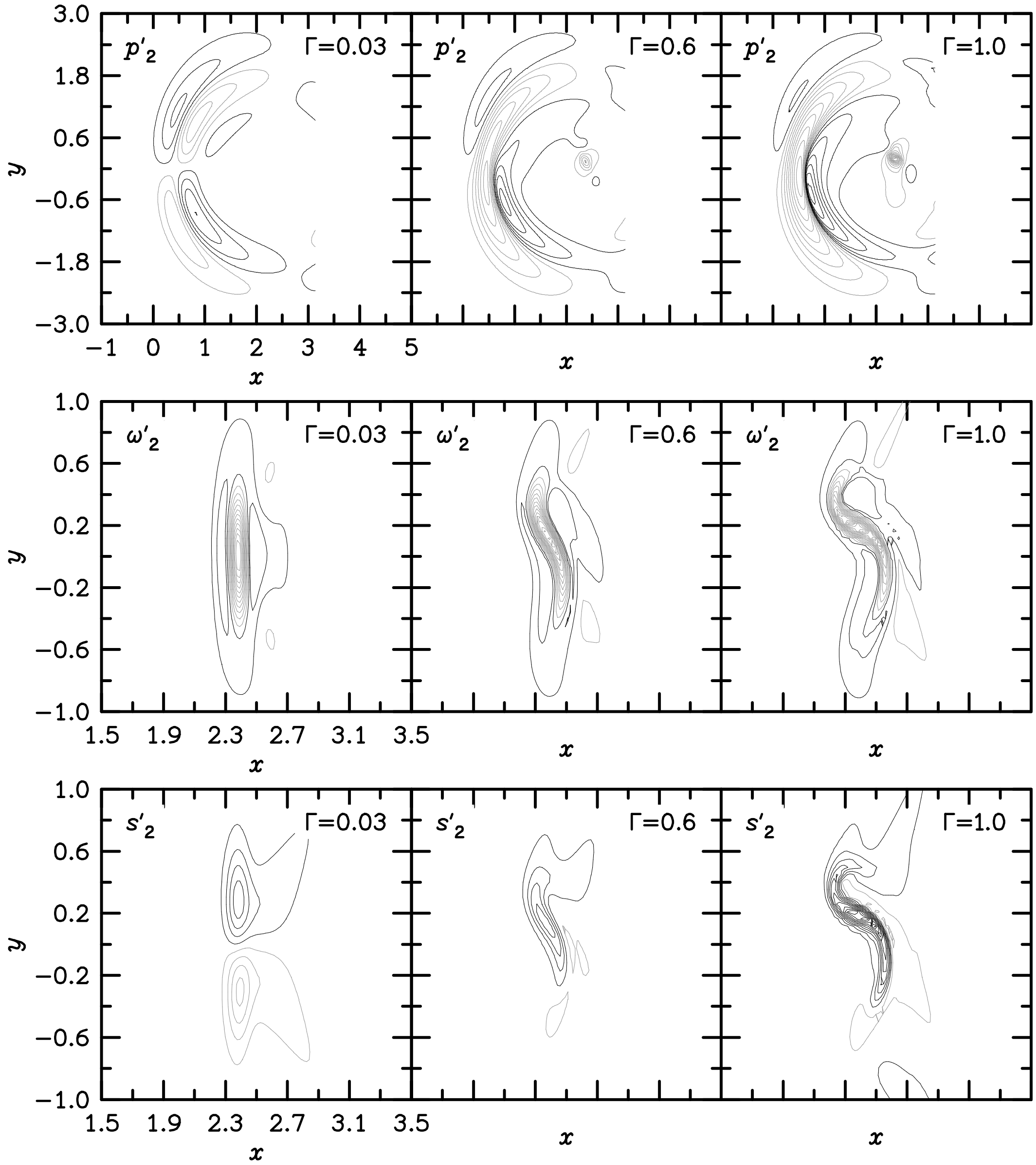

Figure 22: Contour plots of pressure (top row), vorticity (middle row) and perturbation entropy ($\log((p/P)/(\rho/\rho_0)^{\gamma})$) (bottom row) at $\Gamma = 0.03$ (left column), 0.6 (middle column) and 1.0 (right column). $M_1 = 8$. The axis labels are the same across rows.

entropy at $\Gamma = 0.03$ whose contours lie in the range $[-0.002, 0.002]$ to make them visible. The contours are solid if the variable is positive, dotted (gray) otherwise. As the circulation is increased, the pressure perturbation develops an increasingly steep front, which accounts for the increasing dilatation in the time histories presented earlier in Figure 12.

At $M_1 = 8$, the front tends to steepen in the downstream direction, while it steepens in the upstream direction at $M_1 = 2$. The vorticity amplification is a function of the shock Mach number. The entropy, very weak at the low circulation levels, strengthens considerably as the circulation increases, and follows the contours of the vorticity field.

5.1 High Mach Number Expansion

To establish a quantitative criterion for the onset of nonlinear effects, we perform a high Mach number expansion of the linearized Rankine-Hugoniot conditions. We start with Equations (8) and (9) which express the downstream velocity and pressure as a function of upstream variables. For the purpose of linearization, we express all variables as a sum of a mean component and a perturbation. Perturbation variables are denoted by a prime. Mean variables are capitalized except for density which has the subscript m. The downstream velocity, pressure, and density are thus written as

$$\mathbf{u} = (U + u', v'), \tag{57}$$

$$p = P + p', \tag{58}$$

$$\rho = \rho_m + \rho', \tag{59}$$

while the unit normal and tangent vectors to the shock become $\mathbf{n} = (1, -x_{s,y})$ and $\mathbf{t} = (x_{s,y}, 1)$. To first order in the perturbation variables,

$$\mathbf{u} \cdot \mathbf{n} = U + u', \tag{60}$$

$$\mathbf{u} \cdot \mathbf{t} = U x_{s,y} + v'. \tag{61}$$

Substituting (57)-(61) into (8)-(9) and keeping terms linear in the perturbation variables results in the following relations for the downstream perturbation velocity and pressure (we drop the primes):

$$\begin{aligned} u &= u_s + \frac{\gamma-1}{\gamma+1}(u_1 - u_s) + \frac{2\gamma}{\gamma+1}\frac{p_1}{\rho_{1m}U_1}, \\ &- \frac{2\gamma}{\gamma+1}\frac{P_1}{\rho_{1m}U_1}[\frac{\rho_1}{\rho_{1m}} + \frac{u_1 - u_s}{U_1}], \end{aligned} \tag{62}$$

$$v = v_1 - \frac{2\sqrt{\gamma}}{1+\gamma}\, x_{s,y}, \tag{63}$$

$$p = \frac{\gamma-1}{\gamma+1} p_1 + \frac{2}{\gamma+1}[2\rho_{1m} U_1 (u_1 - u_s) + \rho_1 U_1^2]. \tag{64}$$

To scale out the dependence of the upstream variables on circulation, we write $\rho_1 = \Gamma^2 \rho_{10}$, $u_1 = \Gamma u_{10}$, $u_s = \Gamma u_{s0}$, $p_1 = \Gamma^2 p_{10}$. Note that the shock velocity is assumed to have the same scaling with respect to circulation as the upstream perturbation velocity. Using these relations in the above equations, and neglecting all terms $O(1/M_1)$ for large values of M_1, we obtain

$$u = \frac{2\Gamma}{\gamma+1}(u_{s0} + (\gamma-1)u_{10}), \tag{65}$$

$$v = \Gamma(v_{10} - \frac{2\sqrt{\gamma}}{1+\gamma}\, x_{s0,y}), \tag{66}$$

$$p = \frac{2\gamma\Gamma^2 M_1^2 \rho_{10}}{\gamma+1} - \frac{4\Gamma M_1\sqrt{\gamma}}{\gamma+1}(u_{10} - u_{s0}) + \frac{\gamma-1}{\gamma+1}\Gamma^2\, p_{10}. \tag{67}$$

Here, we have used the fact that $U_1 = -\sqrt{\gamma} M_1$, and the upstream mean thermodynamic variables are equal to unity recalling the initial nondimensionalization scheme.

An interesting consequence of (67) is that the downstream pressure loses its quadratic dependence on circulation if there is no density variation in the upstream vortex. In this particular situation, the nonlinear effects are considerably reduced.

To lowest order, the downstream flow velocity components only scale with Γ and not with M_1. The tangential velocity is affected to leading order by the instantaneous shock profile, while the normal velocity is influenced by the instantaneous shock velocity u_s.

Equation (67) indicates that the term linear in Γ dominates the quadratic term for a fixed Γ if

$$\Gamma M_1 < \frac{2}{\sqrt{\gamma}} \left| \frac{u_{s0} - u_{10}}{\rho_{10}} \right|. \tag{68}$$

A plot of this relation is shown in Figure 23; it confirms our earlier conclusion that nonlinear effects (measured by a quadratic dependence of downstream quantities on Γ) are stronger at higher Mach numbers for a fixed value of circulation. Nonlinear effects become noticeable

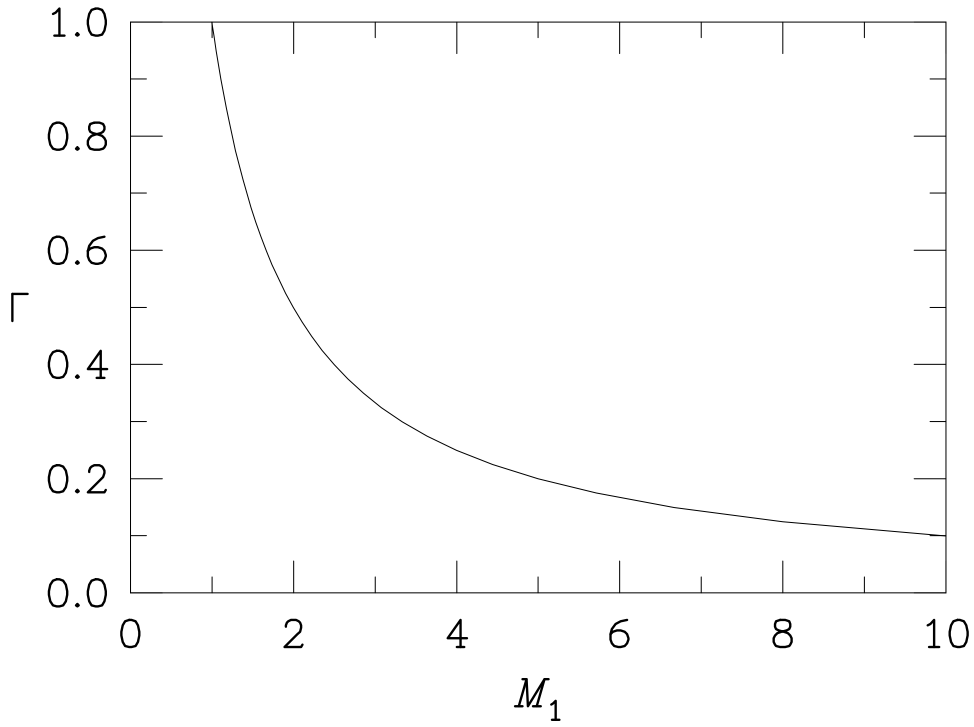

Figure 23: Qualitative nonlinear threshold curve $\Gamma M_1 = 1$.

in the time histories of mean squared quantities when the quadratic contribution is approximately 10 percent of the linear contribution. Therefore, we state that nonlinear effects must be taken into account in any theoretical model if

$$\Gamma M_1 \geq \epsilon \frac{2}{\sqrt{\gamma}} \left| \frac{u_{s0} - u_{10}}{\rho_{10}} \right|, \tag{69}$$

where $\epsilon = 0.1$. We have neglected the shock velocity, although it is of the same order as u_{10}. The specific forms of the upstream density perturbation and velocity (49)-(51) at $r = r_0 = 0.3$ are substituted into Eq. (69) to obtain the criterion for the onset of nonlinearities,

$$\Gamma M_1 \approx 0.9, \tag{70}$$

valid for the specific vortex model studied here. At Mach 2, nonlinear effects contribute approximately 10 percent of the mean square amplitudes when $\Gamma < 0.45$, while the threshold is at $\Gamma = 0.11$ when $M_1 = 8$. These thresholds uphold the earlier simulation results which conclusively demonstrated stronger nonlinear effects (measured by quadratic effects of circulation) at higher Mach numbers.

6 Conclusions

In this paper, we studied the interaction between an infinite plane shock wave and vortical disturbances with a view to delineate the linear regime and explain the onset of nonlinear effects. We solved the two-dimensional compressible Euler equations with a highly accurate, shock-fitted numerical scheme. Comparison of the numerically computed transfer functions with those derived from linear theory along the entire downstream extent show very good agreement even for what may be considered reasonably large upstream wave amplitudes. We also confirmed that the linear theory remains valid as the critical angle is approached from the supercritical side, and substantiated that the time scale over which the flow transients vanish scales as $(\theta - \theta_{cr})^{-1}$. We provided a mathematical explanation of these transient phenomena as due to a zero eigenvalue of the linearized system of equations at the critical angle.

The investigation of nonlinear effects in the case of a shock interacting with a compact vortex indicates that nonlinear effects become more important at higher Mach number for a fixed circulation. Similarly, nonlinearities also become more important as circulation increases for a fixed Mach number. Although the enstrophy was rather insensitive to variation in vortex circulation, the pressure and dilatation were clearly subject to strong nonlinear effects. A high Mach number expansion of the Rankine-Hugoniot conditions led to the conclusion that the strength of nonlinearity could be parameterized by the product of shock Mach number and vortex circulation.

7 Acknowledgements

The authors would like to thank Mark Carpenter, Glenn Lasseigne, and Kristine Meadows for many fruitful discussions.

References

[1] Barre, S., Alem, D., & Bonnet, J.P. 1995 Experimental Study of a Normal Shock/Homogeneous Turbulent Interaction. AIAA Paper No. 95-0579.

[2] Canuto, C., Hussaini, M. Y., Quarteroni, A. & Zang, T.A. 1987 *Spectral Methods in Fluid Dynamics*. Springer Verlag, Berlin.

[3] Carpenter, M.H. & Kennedy, C.A. 1994 Fourth-Order 2N-Storage Runge-Kutta Schemes. NASA Report NASA-TM-109112.

[4] Chang, C.T. 1957 Interaction of a plane shock and oblique plane disturbances with special reference to entropy waves. *J. Aero. Sci.* **24**, 675-682.

[5] Ellzey, J.L., Henneke, M.R., Picone, J.M. & Oran, E.S. 1995 The interaction of a shock with a vortex: shock distortion and the production of acoustic waves. *Phys. Fluids* **7**(1), 172-184.

[6] Erlebacher, G., Hussaini, M.Y. & Shu, C.-W. 1995 Interaction of a shock with a longitudinal vortex. *J. Fluid Mech.* **337**, 129-153.

[7] Jackson, T.L., Hussaini, M.Y. & Ribner, H.S. 1991 Interaction of Turbulence with a detonation wave. *Phys. Fluids A* **5** 745-749.

[8] Kerrebrock, J.L. 1956 The interaction of flow discontinuities with small disturbances in a compressible fluid. Ph.D. thesis, California Institute of Technology.

[9] Kopriva, D.A., Zang, T.A. & Hussaini, M.Y. 1991 Spectral methods for the Euler equations: the blunt body problem revisited. *AIAA J.* **9**, 1458-1462.

[10] Lasseigne, D.G., Jackson, T.L. & Hussaini, M.Y. 1991 Nonlinear interaction of a detonation/vorticity wave. *Phys. Fluids A* **3**(8), 1972-1979.

[11] Lee, S., Lele, S.K. & Moin, P. 1991 Direct numerical simulation and analysis of shock turbulence interaction. AIAA Paper No. 91-0523.

[12] Lee, S., Lele, S.K. & Moin, P. 1993 Direct numerical simulation of isotropic turbulence interacting with a weak shock wave. *J. Fluid Mech.* **251**, 533-562.

[13] McKenzie, J.F. & Westphal, K.O. 1968 Interaction of linear waves with oblique shock waves. *Phys. Fluids* **11**, 2350-2362.

[14] Meadows, K.R., Kumar, A. & Hussaini, M.Y. 1991 Computational study on the interaction between a vortex and a shock wave. *AIAA J.* **29**(2), 174-179.

[15] Meadows, K.R. 1995 A Numerical study of fundamental shock noise mechanisms. Doctoral dissertation. 175 pp.

[16] Moore, F.K. 1953 Unsteady oblique interaction of a shock wave with a plane disturbance. NACA TN-2879. Also, NACA Report 1165.

[17] Naumann, A. & Hermanns, E. 1973 On the interaction between a shock wave and a vortex field. AGARD-CP-131.

[18] Pao, S.P. & Salas, M.D. 1981 A numerical study of two-dimensional shock-vortex interaction. AIAA Paper 81-1205.

[19] Ram, G.S. & Ribner, H.S. 1957 The sound generated by interaction of a single vortex with a shock wave. In *Heat Transfer and Fluid Mechanics Institute*, 1-21. Also, Ribner, H.S. 1959. University of Toronto, Institute for Aerospace Studies, UTIA Report 61.

[20] Ribner, H.S. 1953 Convection of a pattern of vorticity through a shock wave. NACA TN-2864. Also, NACA Report 1164.

[21] Ribner, H.S. 1954 Shock-turbulence interaction and the generation of noise. NACA TN-3255. Also, NACA Report 1233.

[22] Ribner, H.S. 1985 Cylindrical sound wave generated by shock-vortex interaction. *AIAA J.* **23**(11), 1708-1714.

[23] Ribner, H.S. 1987 Spectra of noise and amplified turbulence emanating from shock-turbulence interaction. *AIAA J.* **25**(3), 436-442.

[24] Rotman, D. 1991 Shock wave effects on a turbulent flow. *Phys. Fluids A* **3**(7), 1792-1806.

[25] Saffman, P.G., 1985 Vortex Dynamics. In *Theoretical Approaches to Turbulence*. Eds. D.L. Dwoyer, M.Y. Hussaini, R.G. Voigt, Springer-Verlag, NY, 263-278.

[26] Salas, M.D., Zang, T.A. & Hussaini, M.Y. 1982 Shock-fitted euler solutions to shock-vortex interactions. In *Proceedings of the 8th International Conference on Numerical Methods in Fluid Dynamics,* Ed. E. Krause, Springer-Verlag, NY, 461-467.

[27] Ta'asan,S. & Nark, D. 1995 An absorbing buffer zone technique for acoustic wave propagation. In *33rd Aerospace Sciences Meeting and Exhibit*, Reno NV. AIAA Report 95-0164.

[28] Weeks, T.M. & Dosanjh, D.S. 1965 Interaction of a Starting Vortex as Well as a Vortex Street with a Traveling Shock Wave. *AIAA J.* **3**, NO. 2, 216-223.

[29] Weeks, T.M. & Dosanjh, D.S. 1967 Sound Generated by Shock Vortex Interaction, *AIAA J.*, **5**, 660-669.

[30] Zang, T.A., Hussaini, M.Y. & Bushnell, D.M. 1984 Numerical computations of turbulence amplification in shock-wave interactions. *AIAA J.* **22**(1), 13-21.

Appendix

In this Appendix, we provide the formulas required to compute the transfer functions (based on linear theory) that are used to check the range of validity of linear theory. All variables are nondimensionalized as defined in the paper.

The mean Rankine-Hugoniot conditions that relate upstream and downstream variables are given by

$$M^2 = \frac{2 + M_1^2(\gamma - 1)}{2\gamma M_1^2 - (\gamma - 1)}, \tag{71}$$

$$r = \frac{\rho}{\rho_1} = \frac{U_1}{U} = \frac{(\gamma + 1)M_1^2}{2 + M_1^2(\gamma - 1)}, \tag{72}$$

$$\frac{P}{P_1} = \frac{2\gamma M_1^2 - (\gamma - 1)}{\gamma + 1}. \tag{73}$$

Given the incident angle $\theta < \pi/2$, formed by the wavefront of the incoming vorticity wave with the x axis (measured counterclockwise from the x axis), the angle formed by the wavefront of the downstream vorticity wave and the x axis is given by

$$\cos\theta' = M, \tag{74}$$

while the critical angle is defined by

$$\tan\theta_{cr} = \frac{(1 - M^2)^{1/2}}{rM}. \tag{75}$$

The transfer functions for the perturbation quantities are listed below with no attempt to explain their derivation. The upstream velocity has amplitude ϵU_1. A derivation of these relations is found in Ribner (1953).

<u>Density</u>

$$\rho^2 = M^2\rho_{m1}^2\left[\frac{(\gamma-1)^2(r-1)^4}{r^2}\cos^2\theta\{(a\tan\theta - 1)^2 + b^2\tan^2\theta\} - \frac{2(\gamma-1)(r-1)^2}{r}\cos\theta\sec\theta'\Pi\right](\epsilon U_1)^2 \tag{76}$$

<u>Vorticity</u>

$$\omega^2 = \frac{S^2 k_y^2}{\cos^2\theta'}(\epsilon U_1)^2 \tag{77}$$

<u>Pressure</u>

$$P^2 = \left(\frac{4\gamma^2 r^2}{((\gamma+1)r - (\gamma-1))^2}\,\frac{1}{M_1^2}\,\Pi^2\ \sec^2\theta'\right)(\epsilon U_1)^2 \tag{78}$$

Dilatation

For $\theta < \theta_{cr}$,

$$(\nabla \cdot \mathbf{u})^2 = \frac{k_y^2(\beta_n^2 - 1)^2}{\beta_n^4 \cos^2\theta'}\ \Pi^2\ (\beta^2 + \tan^2\theta')(\epsilon U_1)^2 \tag{79}$$

For $\theta > \theta_{cr}$,

$$(\nabla \cdot \mathbf{u})^2 = \frac{k_y^2(\beta^2 + 1)^2}{(\beta + \tan\theta')^2 \cos^2\theta'}\ \Pi^2\,(\epsilon U_1)^2 \tag{80}$$

Longitudinal Velocity

For $\theta < \theta_{cr}$,

$$\begin{aligned}\frac{u^2}{(\epsilon U_1)^2} &= S^2\cos^2\theta' + \Pi^2[\cos^2\theta' + \beta^2\sin^2\theta'] \\ &+ 2S\Pi\cos\theta'[\cos\theta'\cos(\psi_s - \psi_p) + \beta\sin\theta'\sin(\psi_s - \psi_p)]\end{aligned} \tag{81}$$

For $\theta > \theta_{cr}$,

$$\begin{aligned}\frac{u^2}{(\epsilon U_1)^2} &= S^2\cos^2\theta' + \Pi^2[\cos\theta' - \beta\sin\theta']^2 \\ &+ 2S\Pi\cos\theta'[\cos\theta' - \beta\sin\theta']\cos(\psi_s - \psi_p)\end{aligned} \tag{82}$$

Tangential Velocity

For $\theta < \theta_{cr}$,

$$\begin{aligned}\frac{v^2}{(\epsilon U_1)^2} &= S^2\sin^2\theta' + \Pi^2[\sin^2\theta' + \beta^2\cos^2\theta'] \\ &+ 2S\Pi\sin\theta'[\sin\theta'\cos(\psi_s - \psi_p) - \beta\cos\theta'\sin(\psi_s - \psi_p)]\end{aligned} \tag{83}$$

For $\theta > \theta_{cr}$,

$$\begin{aligned}\frac{v^2}{(\epsilon U_1)^2} &= S^2\sin^2\theta' + \Pi^2[\sin\theta' + \beta\cos\theta']^2 \\ &+ 2S\Pi\sin\theta'[\sin\theta' + \beta\cos\theta']\cos(\psi_s - \psi_p)\end{aligned} \tag{84}$$

The flow angle θ and wavenumber k_y are specified; the remaining functions and constants introduced in (76)-(84) are listed below.

$$\Pi = \begin{cases} [1/(\beta_n r)](C_1^2 + C_2^2)^{1/2} \exp(-k_y \beta x/\beta_n^2) \cos\theta & \text{for } \theta < \theta_{cr}, \\ (C_1/r)(\cos\theta \sin\omega)/\cos\theta'' & \text{for } \theta > \theta_{cr}, \end{cases}$$

$$S = (A^2 + B^2)^{1/2}(1/r)\cos\theta,$$

$$\beta = (|1-\mu^2|)^{1/2}, \qquad \beta_n^2 = 1 - \mu^2 \cos^2\theta', \qquad \mu = M \sec\theta',$$

$$\psi = \delta_p - x k_y (\tan\theta'' - \tan\theta'),$$

$$\psi_s = \delta_s - x k_y \tan\theta', \qquad \psi_p = \delta_p - x k_y \tan\theta'',$$

$$a = \begin{cases} r\frac{CE+DF}{C^2+D^2} & \text{for } \theta < \theta_{cr}, \\ r\frac{C'+GF'}{E'+GD'} & \text{for } \theta > \theta_{cr}, \end{cases}$$

$$b = \begin{cases} r\frac{CF-DE}{C^2+D^2} & \text{for } \theta < \theta_{cr}, \\ 0 & \text{for } \theta > \theta_{cr}, \end{cases}$$

$$\delta_s = \begin{cases} \tan^{-1}(-B/A) & \text{for } \theta < \theta_{cr}, \\ 0 & \text{for } \theta > \theta_{cr}, \end{cases}$$

$$\delta_p = \begin{cases} \tan^{-1}[(C_1\beta - C_2\tan\theta')/(C_2\beta + C_1\tan\theta')] & \text{for } \theta < \theta_{cr}, \\ 0 & \text{for } \theta > \theta_{cr}, \end{cases}$$

$$\theta'' = \begin{cases} -\tan^{-1}[(\mu/\beta_n)^2\cos^2\theta'\tan\theta'] & \text{for } \theta < \theta_{cr}, \\ \theta' - \omega & \text{for } \theta > \theta_{cr}, \end{cases} \tag{85}$$

$$\omega = \cot^{-1}\beta,$$

$$A = \sec\theta' + 2(r-1)\cos\theta' + (a/r)(r-1)^2\sin\theta',$$

$$B = (b/r)(r-1)^2\sin\theta',$$

$$d = 1 - 2\,\frac{\gamma-1}{\gamma+1}\,r,$$

$$C = [d + 2r - 1 - (r-1)/\beta_n^2] \tan\theta' - [(r-1)^2/\beta_n^2] \sin\theta' \cos\theta',$$

$$C' = 1 - d - 2[1 + (r-1)\cos^2\theta'],$$

$$D = \beta D'/\beta_n^2, \qquad D' = (r-1)[1 + (r-1)\cos^2\theta'],$$

$$E = 1 + d + 2(r-1)(\beta^2/\beta_n^2)\cos^2\theta',$$

$$E' = (r-1)^2 \sin\theta' \cos\theta' - (d+r)\tan\theta',$$

$$F = (\beta/\beta_n^2)F', \qquad F' = 2(r-1)\sin\theta' \cos\theta',$$

$$G = \frac{1 - \beta\tan\theta'}{\beta + \tan\theta'},$$

$$C_1 = ar^{-1}D' - F', \qquad C_2 = br^{-1}D'.$$